International Journal of Hydrogen Energy 186 (2025) 151842

Contents lists available at ScienceDirect

International Journal of Hydrogen Energy

journal homepage: www.elsevier.com/locate/he

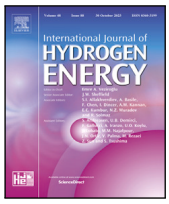

LES analysis of the DLR F400S.3 mGT burner operating with 100% hydrogen fuel

G. Generini [a,*], M. Amerighi [a], T. Lingstädt [b], P. Kutne [b], A. Andreini [a]

[a] Department of Industrial Engineering (DIEF) - University of Florence, Via S. Marta, 3, Florence, 50139, Italy
[b] German Aerospace Center (DLR), Pfaffenwaldring 38-40, Stuttgart, 70569, Germany

ARTICLE INFO

Keywords:
mGT
LES
FGM
PaSR
Hydrogen combustion modeling

ABSTRACT

The paper approaches a computational evaluation of the 100% hydrogen fueled, DLR micro-Gas Turbine (mGT) burner F400S.3 through high-fidelity Large Eddy Simulations (LES). Sensitivity analyses on the thermal boundary conditions of the burner walls and the turbulent combustion model were conducted. The experimental OH*-Chemiluminescence distribution was compared with numerical results obtained using the Partially Stirred Reactor (PaSR) and the Extended Flamelet Generated Manifold (ExtFGM) combustion models. The results showed good agreement regarding the flame shape and reactivity prediction when non-adiabatic thermal boundary conditions were applied at the burner walls and the PaSR model was implemented. On the contrary, the ExtFGM model exhibited underprediction in flame length and flame lift-off, overestimating flame reactivity. Finally, after selecting the combustion model that best retrieved the experimental data, a pressurized LES was performed on the combustor domain to evaluate its performance under real operating conditions for mGT.

1. Introduction

The obligation to minimize the effects of climate change goes hand in hand with assessing the factors driving it. The need to shift towards a climate-neutral economy, thereby reducing polluting emissions, has become crucial and reflects the growing awareness about climate change [1]. To achieve this, a full transition to renewable energy sources and clean energy conversion technologies is essential wherever possible. However, renewable energy sources may not be sufficient to meet the global energy demand on their own, at least for the time being, due to their fluctuating nature and geographical limitations [2].

From this perspective, the use of zero carbon energy carriers such as hydrogen (H_2) has become increasingly significant in facilitating reliable and demand-centered power and heat supply, despite the current lack of large-scale infrastructure for hydrogen transportation. In this context, Combined Heat and Power (CHP) systems have gained relevance, providing high overall efficiency while requiring only a limited amount of H_2, which can be produced locally [3]. micro-Gas Turbines (mGT) have emerged as the preferred choice for these systems due to their low maintenance requirements, high load capability, and fuel flexibility, making them an attractive option for CHP generation [4]. These micro-combined heat and power systems offer numerous benefits to both users and the environment. One of the main advantages is enhanced energy security [5]. In fact, by producing heat and electricity concurrently, micro-CHP systems reduce costs associated with energy distribution infrastructures and minimize energy losses during electricity transmission [6]. Furthermore, power decentralization becomes increasingly relevant, as micro systems are particularly suitable for applications where significant thermal demand is closely linked to the user's electricity demand [7].

However, while the properties of mGTs are well-suited for traditional fuels like natural gas and synthesis gases, the H_2 combustion characteristics present unique challenges that must be carefully evaluated. Indeed, the high inlet temperatures in the combustor, resulting from exhaust gas heat recovery, pose a specific challenge for premixing hydrogen. This is due to its self-ignition characteristics and wide flammable range, which significantly increase the tendency for flashback and auto-ignition [8]. Addressing these technical challenges is thus essential for ensuring safe and reliable operation.

Several studies have investigated hydrogen fueling in mGTs. Calabria et al. [9] achieved 15% H_2 on the AE-T100 Ansaldo Green Tech mGT, highlighting the need for a burner geometrical redesign to mitigate the risk of combustion anomalies onset for higher H_2 concentrations. Cappelletti et al. [10] performed a numerical re-design of the burner, achieving 100% H_2 in simulations while avoiding flashback and self-ignition. Devriese et al. [11] examined, on a different burner,

* Corresponding author.
E-mail address: giulio.generini@unifi.it (G. Generini).

https://doi.org/10.1016/j.ijhydene.2025.151842
Received 25 February 2025; Received in revised form 1 October 2025; Accepted 2 October 2025
Available online 20 October 2025

how the fuel nozzle geometry and flame stabilization method influence NO_x emissions. Similarly, Hohloch et al. [12] emphasized the impact of flame stabilization on the risk of self-ignition and flashback in the mixing zone, recommending jet-stabilized combustion systems over swirl-stabilized ones for H_2 fueled mGT burners.

In this context, numerous studies in the literature investigate the MILD combustion regime [13], showing higher performances regarding hydrogen flames avoiding flashback propensity with high momentum jet-stabilized type of combustors [14,15]. Additionally, NO_x emissions are minimized due to an inner large recirculation region that stabilizes the flame in the combustion chamber, combined with short residence times resulting from the high-velocity jets [16–18].

Various strategies have been developed to model the combustion process, each based on different assumptions about how chemical reactions are treated. These strategies range from cost-efficient methods, such as tabulated chemistry approaches, to more numerically-expensive models that directly account for species transport.

A promising solution within the tabulated chemistry approach is the Flamelet Generated Manifolds (FGM) model [19], which optimizes the computational process by generating a look-up table in an initial step, derived from the resolution of multiple laminar flamelets. In this framework, the thermodynamic states are characterized as functions of two key control variables: the mixture fraction Z and the progress variable c. This allows for a more efficient representation of the complex combustion process while maintaining accuracy. Although the FGM model offers lower computational costs due to fewer transport equations, it does not inherently account for the preferential diffusion effects characteristic of lean H_2 flames [20], which introduces limitations specifically for hydrogen combustion [21]. Moreover, the traditional FGM model does not consider stretch and non-adiabatic effects on the flame reactivity during the tabulation process. Despite the use of the traditional FGM model being the standard in many studies [22–25], many works could be found in the literature focusing both on introducing an extension to the model to take into account the non-Unity Lewis number effects within H_2 flames [26–29] and to acknowledge the influence of stretch and heat loss and gain on flame topology [30–34].

The second strategy to address turbulent flames involves solving a transport equation for each species included in the selected chemical reaction mechanism. This species transport approach provides a detailed representation of flame chemistry and captures preferential diffusion effects in H_2 flames. However, it significantly increases computational cost due to the large number of transport equations, which scales with the number of species. To address these challenges in the context of turbulence-chemistry interactions, models such as the Partially Stirred Reactor (PaSR) [35–38], and the Thickened Flame (TF) model (in the LES framework) [39,40] are commonly employed.

This work aims to numerically investigate the German Aerospace Center (DLR) mGT burner F400S.3 [12], focusing on evaluating the performance of an extended tabulated chemistry-based model against species transport-based model on a lean hydrogen flame under both adiabatic and non-adiabatic thermal boundary conditions. High-fidelity Large Eddy Simulations (LES) were conducted to assess the final sensitivity analyses. It is important to note that, to the author's knowledge, no high-fidelity studies have been published in the literature specifically addressing this burner, nor have they evaluated the effects of turbulent combustion models and non-adiabatic boundary conditions on its performance. Initially, a preliminary RANS Conjugate Heat Transfer (CHT) analysis of the burner was performed to compute the combustor wall temperature distributions, which were then used as boundary conditions for the LES. The consideration of non-adiabatic boundary conditions is crucial due to the burner's geometry: neglecting fluid-solid heat transfer could lead to an underestimation of both temperature and velocity within the combustion chamber. This issue is particularly relevant for the reverse-flow type of combustor characteristic for micro-Gas Turbines [41]. Subsequently, the Flamelet Generated Manifolds (FGM) and the Partially Stirred Reactor (PaSR) combustion models were evaluated on the burner by comparing the CFD results with the experimental OH*-Chemiluminescence data. Specifically, a new formulation for the FGM model (Extended FGM), previously presented by the authors in [41], was here implemented, accounting for the stretch and non-adiabatic effects of the flame. Then, once the computational setup that best replicated the experimental results was identified, the burner was also analyzed at an elevated pressure (approximately 4.5 bar) to assess its performance under representative operating conditions for a commercial micro gas turbine (mGT).

2. Combustion models

2.1. Extended Flamelet Generated Manifolds (ExtFGM)

The Flamelet Generated Manifold (FGM) model is a tabulated chemistry-based approach funded on the idea that the chemical state only depends on two control variables, the mixture fraction Z and the progress variable c [42]. The mixture fraction Z represents the local composition of the mixture, while the progress variable c indicates the global reaction progress towards equilibrium, modeling the combustion process as a single-step reaction with a characteristic time scale. Z is computed through Bilger's definition [43], while c is estimated as ratio of a linear combination of the H_2O and H_2 mass fractions to their values at local equilibrium [44]:

$$c = \frac{Y_{H_2O} - Y_{H_2}}{(Y_{H_2O} - Y_{H_2})_{eq}} \tag{1}$$

By solving premixed mono-dimensional laminar flamelets, a look-up table is created to describe the complete space of the two control variables, through $Z \mathrm{x} c = 64 \times 32$ points. The DC1S09 chemical scheme, developed by the German Aerospace Center (DLR), characterized by 9 species and 23 reactions, is used to solve the laminar flamelets. The DC1S09 is a skeletal mechanism for H_2 combustion, obtained from the DLR Concise (238 species and 1814 reactions), developed for jet fuels [45]. Lastly, to take into account the influence of turbulence on chemistry, a β-shaped Probability Density Function (β-PDF) is assumed a priori for the two variables. As a result, the integrated value of a generic turbulent quantity $\tilde{\varphi}$ can be expressed as:

$$\tilde{\varphi}(\tilde{Z}, \tilde{c}, \widetilde{Z''^2}, \widetilde{c''^2}) = \iint \varphi(c, Z) PDF(c, \tilde{c}, \widetilde{c''^2}) PDF(Z, \tilde{Z}, \widetilde{Z''^2})\, dc\, dZ \tag{2}$$

where $\tilde{Z}, \tilde{c}$ and $\widetilde{Z''^2}, \widetilde{c''^2}$ are the mean values and variances of mixture fraction and progress variable, respectively, and $\varphi(c, Z)$ the value extracted from the laminar look-up table.

As mentioned, the traditional FGM model cannot natively take into account the preferential diffusion effects with only two control variables (Z and c) [28]. Moreover, the model struggles to correctly predict flame morphology where the flame stretch and non-adiabatic effects are predominant [30]. Thus, an enhanced version of the FGM model is further here applied to account for these effects without modifying the governing equations. The model improvement is performed by multiplying the standard progress variable source term $\bar{\omega}_c$ by a correction factor Γ, following the work originally introduced, in the RANS framework, by Klarmann et al. [33]. A LES validation of the model has been performed in the work by Langone et al. [34].

The reaction progress source term results in:

$$\bar{\omega}_c = \Gamma(Z, \beta, \kappa) \bar{\rho} \iint \frac{\dot{\omega}_c(Z, c)}{\rho(Z, c)} P\tilde{D}F(Z, c) dZ dc \tag{3}$$

with Γ:

$$\Gamma(Z, \beta, \kappa) = \left(\frac{S_c(Z, \beta, \kappa)}{S_c^0(Z)} \right)^m \tag{4}$$

Here, S_c denotes the non-adiabatic, stretched fuel consumption speed, while S_c^0 represents the adiabatic, unstretched consumption speed, commonly referred to as the laminar flame speed. The term κ

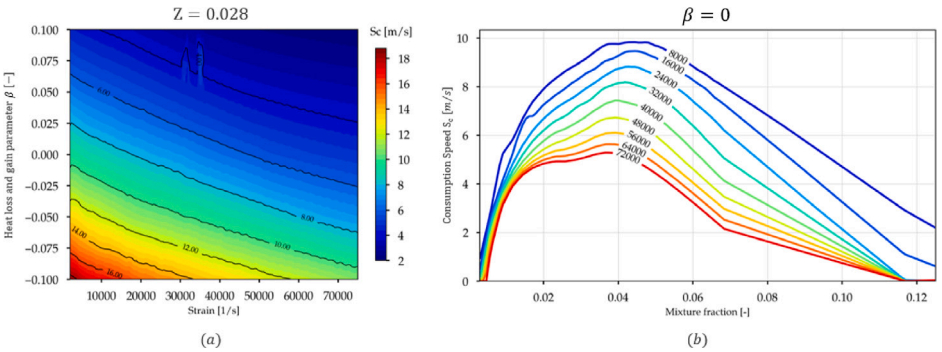

Fig. 1. Laminar consumption speed as a function of (a) strain rate [1/s] and heat loss/gain parameter at a fixed stoichiometric mixture fraction, and (b) strain rate [1/s] and mixture fraction under adiabatic conditions ($\beta = 0$). The values are defined for H_2/air flames, corresponding to the atmospheric test case boundary conditions for the air and fuel temperatures.

corresponds to the flame stretch, and β accounts for heat losses and gains. Finally, m is a proportionality factor linking the consumption speed S_c to the mean progress variable source term $\bar{\omega}_c$, as described in [33].

To compute S_c, a consumption speed $S_c(Z, \beta, \kappa)$ look-up table is generated during a pre-processing step by evaluating the effects of stretch and heat loss/gain on laminar flames. This is accomplished by solving mono-dimensional laminar premixed counterflow flames in a 'fresh-to-burnt' configuration. The simulations employ the Cantera v2.6.0 Python libraries [46], solving H_2/air flames using the skeletal reaction mechanism DC1S09. A full multicomponent formulation for species diffusion is adopted to account for non-unity Lewis numbers in the laminar flame solution.

A key consideration in this process is the treatment of flame stretch, which, by definition, comprises both strain and curvature. Since curvature is inherently a three-dimensional phenomenon and this phase of the study is restricted to one-dimensional flames, it is excluded. Consequently, strain alone is used to represent the total stretch.

The flame response to various degrees of flame strain was analyzed by increasing the reactants' and products' jet velocities until either a maximum specified level of strain was achieved or the flame extinction occurred. On the other side, the flame's behavior under different levels of heat loss and gain was analyzed by respectively decreasing or increasing the unburnt mixture and products' total enthalpy with respect to the adiabatic condition, employing the parameter β. To clarify, $\beta = 0$ denotes the adiabatic condition, $\beta > 0$ indicates the presence of heat loss, and $\beta < 0$ emphasizes the effect of heat gain. Further information on κ and β formulations could be found in the work by Generini et al. [41].

Therefore, the consumption speed S_c is evaluated for every flame through Poinsot and Veynante's expression [47]:

$$S_c = \frac{1}{\rho_u \Delta H_c^0 Y_f} \int_{-\infty}^{\infty} \dot{q} dx \tag{5}$$

where ρ_u represents the unburnt mixture density and $\dot{q}$ the total heat release rate per unit volume. Fig. 1 shows the effects of these variables on the consumption speed, considering the stoichiometric composition (a) and the adiabatic case (b), computed for the case-specific boundary conditions.

Subsequently, the evaluated consumption speed is stored in a look-up table, which is accessed at runtime via a dedicated subroutine written in C during the CFD simulation. This routine performs interpolation based on three parameters: the heat loss/gain parameter β, the total flame stretch κ_{tot}, and the mixture fraction Z, each calculated within every computational cell. Notably, in the three-dimensional simulation framework, the look-up table is indexed using the total stretch rate rather than just the strain rate, allowing curvature effects to be taken into account and enabling the incorporation of curvature-induced variations.

That said, the total flame stretch κ_{tot} is evaluated within the routine using the following component-wise formulation:

$$\kappa = \underbrace{(\delta_{ij} - \widetilde{n_i n_j})\frac{\partial \tilde{u}_i}{\partial x_j}}_{\kappa_{mean}} + \underbrace{\Gamma_k \left(\frac{u'}{S_c^0}, \frac{l_t}{\delta_L^0} \right) \frac{\epsilon}{k}}_{\kappa_{turb}} + \underbrace{S_L^0 \frac{\frac{1}{2} - \bar{c}}{l_w}}_{\kappa_{curv}} \tag{6}$$

The mean-flow-induced stretch κ_{mean} is calculated using the Kronecker delta δ_{ij} and the orientation tensor $\widetilde{n_i n_j}$, following the formulation proposed by Veynante et al. [48,49]. The turbulent contribution to flame stretch, κ_{turb}, captures the effect of flame front wrinkling induced by turbulent velocity fluctuations. It is modeled using the Intermittent Turbulence Net Flame Stretch (ITNFS) framework introduced by Meneveau and Poinsot [50], incorporating the influence of both turbulent and chemical time and length scales through the efficiency function Γ_k.

The curvature-induced stretch term, κ_{curv}, accounts for changes in local flame propagation speed due to front curvature. Here, S_L^0 denotes the unstretched laminar flame speed, and l_w is a characteristic length scale representing the wavelength of flame wrinkles within the turbulent flame brush, as defined by Bray et al. [51].

For a more detailed discussion of the heat loss/gain parameter β, the reader is referred to [41].

Using the local values of flame stretch κ, heat-loss/gain parameter β, and mixture fraction Z, a linear interpolation is applied to the look-up table in order to compute, at runtime and for each cell in the domain, the corresponding consumption speed and, consequently, the correction factor Γ. This strategy ensures consistency with the local thermochemical and flow conditions throughout the simulations.

Linear interpolation was deliberately chosen over more sophisticated schemes for several reasons. First, it provides a balanced compromise between computational cost and accuracy. Since interpolation is performed at every time step and in every computational cell, higher-order methods would significantly increase the computational overhead, potentially making the simulations impractical under realistic time and resource constraints. Second, the look-up table itself is densely populated, with a large number of discretized points, each obtained from a fully resolved counterflow flame calculation. This fine resolution captures the one-dimensional flame behavior across a broad range of operating conditions. In this context, linear interpolation is sufficiently accurate, as the dense sampling minimizes interpolation errors while keeping the approach computationally efficient.

2.2. Partially Stirred Reactor (PaSR)

The Partially Stirred Reactor (PaSR) is a finite-rate chemistry model based on the idea that combustion takes place within reactive structures, referred to as "fine scales", which occupy part of the computational cell volume [52]. The model is generally used for cases where the high dilution levels and the intense mixing between reactants and

combustion products lead to a distributed reaction process, resulting in high Reynolds and moderate Damköhler numbers [53]. In this regard, many works could be found in the literature, both in the RANS [35,54] and LES [55,55,56] frameworks, regarding the application of the PaSR model for evaluating MILD combustion regimes [57]. In the PaSR model, each computational cell could be split into two zones: the reacting (fine-scales) and non-reacting zones. The reaction rate, for a generic species i, is based on the mass exchange between the two regions and is defined as:

$$\bar{\omega}_i = k\frac{\bar{\rho}\left(Y_i^* - Y_i^0\right)}{\tau^*} \tag{7}$$

where Y_i^0 and Y_i^* are the mass fractions for the i-species in the non-reacting and reacting region respectively, $\bar{\rho}$ is the Reynolds-averaged density, τ^* is the fine-scales residence time and k represents the reactive fraction of the cell, thus the fine-scales volume. k is computed as a function of the chemical time scale τ_c and the mixing time scale τ_{mix}:

$$k = \frac{\tau_c}{\tau_c + \tau_{mix}} \tag{8}$$

where τ_c is estimated for every single species included in the chemical reaction mechanism chosen (DC1S09 from DLR), by computing the highest limiting value of the ratio:

$$\tau_{c,i} = \frac{Y_i^*}{dY_i^*/dt} \tag{9}$$

where the lower term identifies the species formation rate in the reactive zone [55].

The mixing time scale is computed as the geometrical mean of the sub-grid velocity stretch time, given by (Δ/v'), and the Kolmogorov time scale, expressed as $((\nu/\epsilon_{sgs})^{1/2})$ [53]. The sub-grid quantity Y_i^* is obtained by considering the reactive zone evolving from Y_i^0 during the simulation time step. The presented formulation pertains to the LES framework: further information regarding the RANS PaSR formulation can be found in the work of Ferrarotti et al. [35], referring to the τ_{mix} expression based on the concept of fractal structures in turbulence, which builds upon the earlier work presented by Golovitchev et al. [58].

3. Atmospheric case

The section presents the atmospheric analysis of the burner. Initially, the experimental test rig is described, followed by a detailed examination of the computational domain characteristics. This includes an overview of the setup for both RANS and LES. Finally, the results from the various sensitivity analyses discussed throughout the section are presented and analyzed.

3.1. Experimental test-rig

The test case considered in this work is the F400S.3 burner, illustrated in Fig. 2, developed at the German Aerospace Center (DLR) in Stuttgart and specifically designed for the Ansaldo Green Tech AE-T100 micro Gas Turbine (mGT). The burner is a reverse-flow, single-can, tubular, atmospheric combustor. The naming convention of the burner is intentional: the "F" signifies the use of FLOX® technology [61], while the number following it, 400, indicates the burner's fuel power rating in kW. The "S" denotes the burner's original design for synthetic gas applications. The latest version, identified with the number 3, has demonstrated versatility in handling a variety of hydrogen-enriched fuel mixtures, with hydrogen content ranging from 0% to 100%, as shown in the work of Hohloch et al. [12]. This adaptability extends the burner's capability beyond its initial purpose, making it suitable for a broader range of hydrogen-based combustion applications.

The burner combustion process operates on a two-stage system comprising a swirl-stabilized pilot stage and a jet-stabilized main stage. The pilot stage employs a diffusive flame, which is primarily utilized

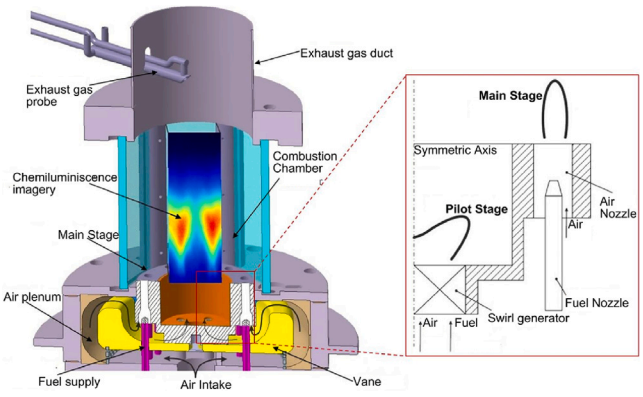

Fig. 2. F400S.3 experimental burner: sectional view (left) of the entire combustor assembly and a detailed view (right) illustrating the fuel injection mechanism for both the swirl-stabilized pilot stage and the jet-stabilized main stage. Adapted from [59,60].

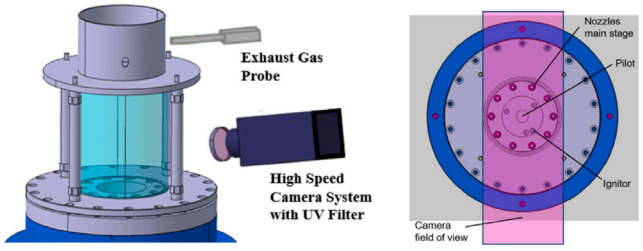

Fig. 3. Representation of the experimental test-rig set-up (left) and horizontal burner section showing the camera field of view (right). Adapted from [12].

during the mGT start-up and to stabilize the main flame, which is technically-premixed. Under optimal design conditions, this main stage processes approximately 90% of the fuel power [2]. A specific flow field is generated within the combustion chamber, characterized by a large inner recirculation zone due to the high axial momentum of the main jets. This design allows combustion products from both the pilot and the main flame to be recirculated back into the main flame reaction zone. By minimizing the formation of low-velocity regions, the burner effectively reduces the risks of flashback and auto-ignition, thus ensuring a more reliable and efficient combustion process.

Fig. 3 presents a schematic of the atmospheric test rig, along with a horizontal cross-section of the combustion chamber, highlighting the camera's field of view. Notably, an exhaust gas probe is positioned at the burner outlet to facilitate flue gas composition analysis.

Further details on the experimental setup can be found in [12].

3.2. RANS and LES simulations set-up

The Navier–Stokes equations were solved using the pressure-based solver ANSYS Fluent 2024 R1 [42] to model the burner domain through both RANS and LES simulations. Fluid-RANS and RANS Conjugate Heat Transfer (CHT) analyses were performed, with the latter specifically used to compute the burner's wall temperature distributions. These temperature profiles were then applied as non-adiabatic thermal boundary conditions in the LES calculations, eliminating the need for a computationally expensive high-fidelity fully coupled CHT analysis.

Both the RANS-CHT and LES simulations were conducted on a 72° sector of the full combustor, leveraging the periodicity of the burner to reduce computational cost and simulation time by modeling only 1/5 of the total geometry (Fig. 4(a)).

The CHT computational grid, illustrated in Fig. 4(b), consists of approximately 1.4E7 polyhedral cells, with 5 layers of prism adjacent to solid walls. The LES grid, which is also used for the fluid

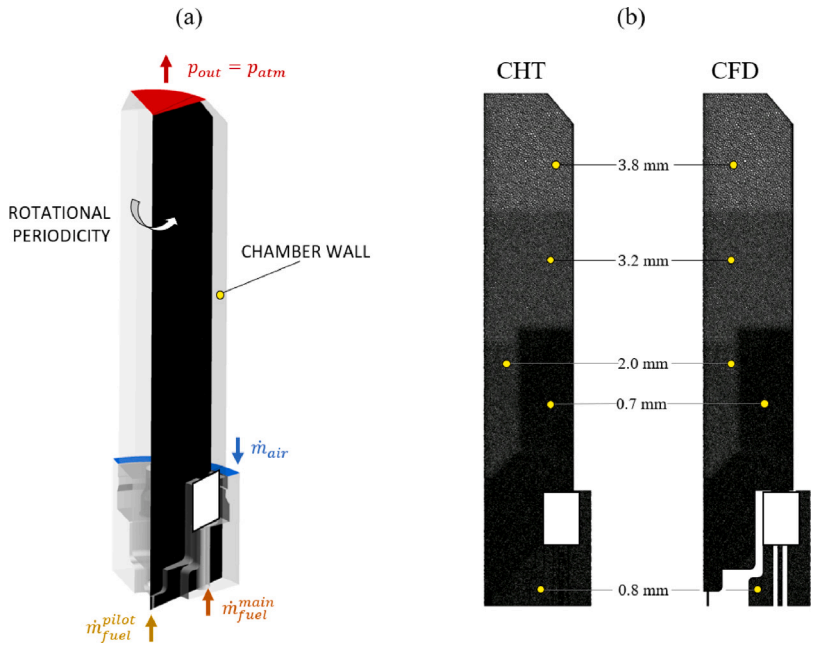

Fig. 4. (a) Computational domain and numerical boundary conditions. (b) Computational grid for the RANS CHT analysis and for the atmospheric LES analysis.

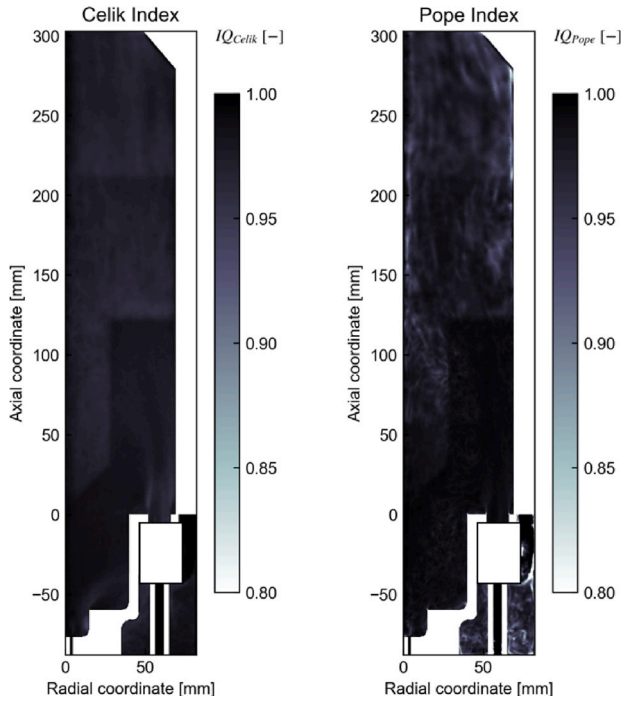

Fig. 5. Contour of time-averaged (left) Celik Index [62] and (right) Pope Index [63] for the LES computational grid.

RANS simulations, was developed using a similar procedure, simply neglecting the solid domain in the CHT grid: a polyhedral mesh of about 1.1E7 cells was computed. To assess the validity of the mesh for the LES calculation, the Celik index [62] and the Pope index [63] were evaluated. As shown in Fig. 5 both indexes appears above the recommended value ($IQ > 0.8$) in the whole domain which ensures proper turbulence resolution.

Equal boundary conditions were set for both the LES and RANS (fluid and CHT) analyses. The overall fuel mass flow was distributed between the main and pilot lines by setting mass flow inlet conditions on their respective inlet surfaces (Fig. 4(a)). Additionally, a mass flow inlet condition was specified for the burner air inlet, along with an atmospheric pressure condition for the burner outlet. For the fluid RANS simulation, adiabatic wall conditions were applied, enforcing a zero heat flux at the boundaries. For the RANS CHT analysis, the wall thermal boundary conditions are a direct output of the calculation, since a direct coupling between the fluid and solid domain is performed by the solver. A temperature-dependent polynomial was set for the solid cell zone material properties. Moreover, the combustion chamber wall (Fig. 4(a)) was modeled as a shell conduction wall [42], with quartz material properties implemented as temperature-dependent polynomials [64].

To account for the cooling effect of the external airflow on the quartz wall, induced by an outlet fan, forced convection was incorporated into the model. The external Heat Transfer Coefficient (HTC) was calculated using the Churchill and Bernstein correlation [65]:

$$Nu = 0.3 + \frac{0.62 Re^{1/2} Pr^{1/3}}{[1 + (0.4/Pr)^{2/3}]^{1/4}} \left[1 + \left(\frac{Re}{282000}\right)^{5/8}\right]^{4/5} \quad (10)$$

where Re and Pr are respectively the Reynolds and Prandtl numbers.

In contrast, for the LES calculation, the wall temperature distributions obtained from the CHT analysis were applied as thermal boundary conditions.

The k-ϵ Realizable model with Enhanced Wall Treatment [42] was used for the RANS simulations, along with the COUPLED solution algorithm for pressure-velocity coupling. Pressure gradients were approximated using a second-order scheme, while all other equations were discretized with a second-order upwind.

In the RANS framework, turbulence-chemistry interaction was exclusively modeled using the Partially Stirred Reactor (PaSR) model, utilizing the skeletal DC1S09 mechanism to describe the system's reactivity.

In the LES context, the effect of unresolved eddies is modeled using the Dynamic Smagorinsky-Lilly formulation, which dynamically evaluates the Smagorinsky constant. The SIMPLEC algorithm was adopted for the pressure-velocity coupling with a constant time step of 5E-6 s, ensuring a convective Courant number, in the region of interest, below 5. Second-order schemes were used for spatial and temporal discretization, with an implicit formulation applied for the latter.

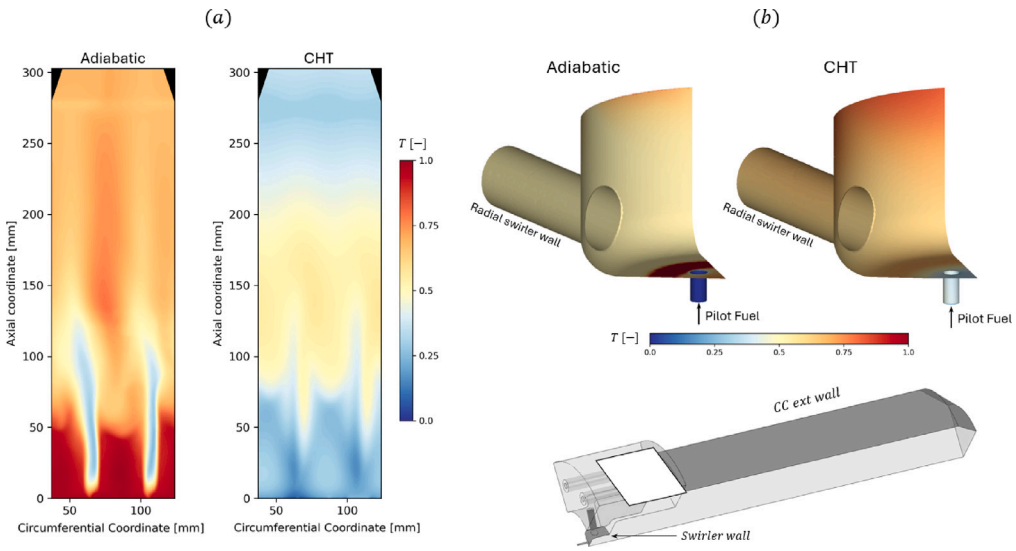

Fig. 6. (a) Normalized temperature distribution across the external wall of the combustion chamber, comparing both the adiabatic CFD and CHT simulations. (b) Normalized temperature distribution on the swirler and pilot flame wall regions, for both the adiabatic CFD and CHT simulations. The temperature values are normalized with respect to the geometry-specific maximum temperature.

The turbulence-chemistry interaction was modeled using the turbulent combustion models presented in Section 2: the ExtFGM and the PaSR, following the formulation presented and employing, once again, the DC1S09 chemical reaction mechanism.

3.3. Results and discussion

3.3.1. RANS results

As discussed earlier, RANS-CHT analyses were carried out to determine the wall temperature distributions, which served as thermal boundary conditions for the LES simulations. Fig. 6 presents the normalized temperature distributions on two critical surfaces: (a) the external surface of the combustion chamber (CC ext wall) and (b) the radial swirler duct wall (Swirler Wall), including a section of the pilot flame region wall.

A detailed comparison is provided for both surfaces, highlighting the differences in wall temperature distributions obtained from the adiabatic CFD simulation and the Conjugate Heat Transfer (CHT) analysis.

Fig. 6(a) displays the external combustion chamber wall projected onto a plane, where the circumferential coordinate is represented as the product of the surface radius and the angular position.

Here, the impact of neglecting heat transfer effects in the adiabatic simulation is evident, leading to significantly higher wall temperatures. Indeed, when heat conduction and forced convection effects on the external wall are accounted for in the Conjugate Heat Transfer (CHT) analysis, the temperature distribution undergoes a notable shift, resulting in overall lower wall temperatures.

This inclusion of heat transfer mechanisms causes the region of peak temperature to move axially downstream, towards the burner outlet, compared to the adiabatic case. In contrast, the adiabatic analysis predicts the highest temperatures at axial coordinates below 50 mm, where the quenching effect induced by heat transfer is not adequately captured. This highlights the importance of incorporating detailed thermal interactions to accurately represent the thermal behavior of the system.

A similar conclusion can be drawn from the temperature distribution presented in Fig. 6(b). The inclusion of heat transfer effects in the solution results in significantly higher wall temperatures on the radial swirler compared to the adiabatic simulation. This finding is particularly noteworthy as the increased wall temperature directly impacts the flow temperature, thereby altering flame characteristics and combustion dynamics.

Notably, the elevated temperature on the wall of the pilot flame region emphasizes the critical influence of heat transfer in stabilizing and shaping the flame. Furthermore, the CHT analysis reveals a higher wall temperature in the pilot fuel adduction duct, which leads to pre-heating of the fuel, which is absent in the adiabatic scenario.

It is worth emphasizing that, even at the RANS analysis level, the significance of heat transfer effects is evident and highly relevant. This aspect, particularly its influence on flow behavior and flame dynamics, will be further examined in Section 3.3.2, with LES calculations.

3.3.2. LES results

The impact of non-adiabatic boundary conditions is evaluated comparing the experimental OH*-Chemiluminescence distribution with the normalized mean HRR integrated along the Line of Sight (LOS) axis, depicted in Fig. 7(a). In the figure, the green arrow indicates the direction of LOS axis movement, while the yellow line represents the axis itself. On the contrary, Fig. 7(b) presents the comparison between the numerical and experimental results. The HRR normalization was carried out using a common global maximum, ensuring a consistent basis for comparison across different cases. In the experiments, normalization was carried out by considering the maximum value within the experimental distribution.

As shown, when non-adiabatic boundary conditions are applied, local flame quenching occurs in specific regions, preventing the flame from anchoring at the nozzle rim and consequently increasing the flame lift-off distance. This could be better explained by evaluating Table 1, which presents the flame lift-off height (LOH) and flame length obtained under both adiabatic and non-adiabatic boundary conditions. Specifically, the flame lift-off height (LOH) is determined as the axial position where 10% of the global light emission is reached, following the methodology described in [66,67]. Similarly, the flame length is evaluated as the axial range between two points corresponding to 10% of the global light emission.

The table results show that the flame lift-off height increases when non-adiabatic boundary conditions are applied, bringing the simulation results closer to the experimental observations. In contrast, the flame length appears to be largely independent of the thermal boundary conditions, retrieving similar results.

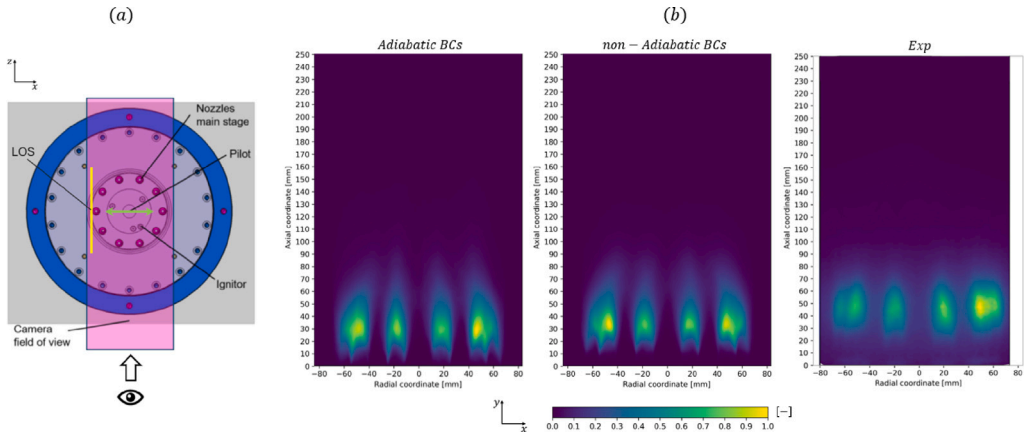

Fig. 7. (a) Horizontal burner section showing the camera field of view [12]. (b) LES-calculated LOS integrated equivalent (HRR) with PaSR model and adiabatic and non-adiabatic thermal boundary conditions, and Experimental OH*- Chemiluminescence.

Table 1
Flame lift-off height (LOH) and length obtained from the atmospheric LES calculations using the PaSR model, under both adiabatic and non-adiabatic thermal boundary conditions, compared with experimental data.

	LOH [mm]	Length [mm]
PaSR adiabatic	7	69
PaSR non-adiabatic	12	69
Exp	16	70

Table 2
Flame lift-off height (LOH) and length obtained from LES calculations using the ExtFGM and the PaSR, under non-adiabatic thermal boundary conditions, compared with experimental data.

	LOH [mm]	Length [mm]
ExtFGM non-adiabatic	10	20
PaSR non-adiabatic	12	69
Exp	16	70

To quantitatively assess the effect of heat losses, the total wall heat flux was computed over all solid boundaries where non-adiabatic boundary conditions were applied as:

$$Q_{\text{wall}} = \int_{S_{\text{wall}}} \overline{q''_{\text{wall}}}\, dS \tag{11}$$

where $\overline{q''_{\text{wall}}}$ represents the local wall heat flux.

Moreover, the total flame power, defined as the volume-integrated chemical heat release, was calculated as:

$$Q_{\text{flame}} = \int_{V} \overline{\dot{q}_{\text{chem}}}\, dV \tag{12}$$

where $\overline{\dot{q}_{\text{chem}}}$ represents the chemical heat release rate per unit volume.

The ratio of these quantities gives a global heat-loss fraction of approximately 6%, indicating that, while the overall impact of heat loss is moderate, it is sufficient to influence flame stabilization.

The effect of non-adiabatic boundary conditions is particularly evident when analyzing the normalized mean temperature distribution on the midplane, especially in the region where the flame stabilizes, as illustrated in Fig. 8. To facilitate the comparison, a common maximum was used for normalization. Furthermore, an isoline of Heat Release Rate (HRR) is plotted to clearly delineate the reactive zone, together with a dotted green isoline corresponding to zero axial velocity to identify the boundaries of the recirculation regions, specifically the inner recirculation zone (IRZ) and the outer recirculation zone (ORZ).

In the ORZ, specifically at the corner of the combustion chamber, the lower temperature leads to an increased flame lift-off compared to the adiabatic case. However, the higher temperature in the IRZ causes the flame to bend towards the burner axis. This increased temperature in the IRZ results from the products of the pilot flame, which are hotter due to solid-fluid heat transfer. Indeed, computing the normalized mean temperature on a plane slicing through the radial swirler reveals that the air temperature rises before entering the combustion chamber (in the Radial Swirler wall previously depicted in Fig. 6), as shown in Fig. 9. This results in a high reactivity pilot flame and, consequently, in a "bent" partially-premixed main flame.

Thus, due to the specific configuration of the burner, heat transfer effects play a crucial role in determining the flame topology. The reverse-flow configuration of the burner leads to a mixture temperature increase before entering the combustion chamber, which ultimately influences the flame characteristics.

After establishing the necessity of incorporating non-adiabatic boundary conditions, the subsequent LES simulations were performed using the previously determined temperature distributions on the combustor walls. These simulations were specifically designed to conduct a sensitivity analysis of the turbulence-chemistry interaction by comparing two distinct modeling approaches.

In this context, a comparison was made, once again, between the experimental OH*-Chemiluminescence distribution and the normalized mean HRR integrated along the LOS axis for all turbulent combustion models (ExtFGM and PaSR), using a common HRR maximum for normalization (Fig. 10).

The results also in terms of flame LOH and length are reported in Table 2.

As mentioned, the extension of the FGM model, presented in Section 2.1, introduces the effects of flame heat loss and gain, as well as flame stretch. From the previous analyses, it is clear that accounting for heat transfer within the domain is fundamental to accurately capture the correct flame topology. However, despite these adjustments, the ExtFGM model still fails to accurately describe the experimentally observed flame topology. The flame appears to be close to the nozzle rim assuming a higher flame reactivity, which brings the flame to be more compact and thus shorter (Fig. 10(a)): from Table 2, the model both underestimates the flame lift-off height and the flame length compared to the experimental data. This is due to various reasons, all of which are related to the inherent characteristics of the FGM.

First, the model does not account for the influence of flame products on the technically premixed flame, in terms of mixture composition. The model chemistry tabulation is inherently not able to address the effect of a different oxidant composition for the main flame, which is determined by the turbulent flow field. The inner recirculation region brings the products from both the pilot and the main flame into direct interaction with the main flame itself.

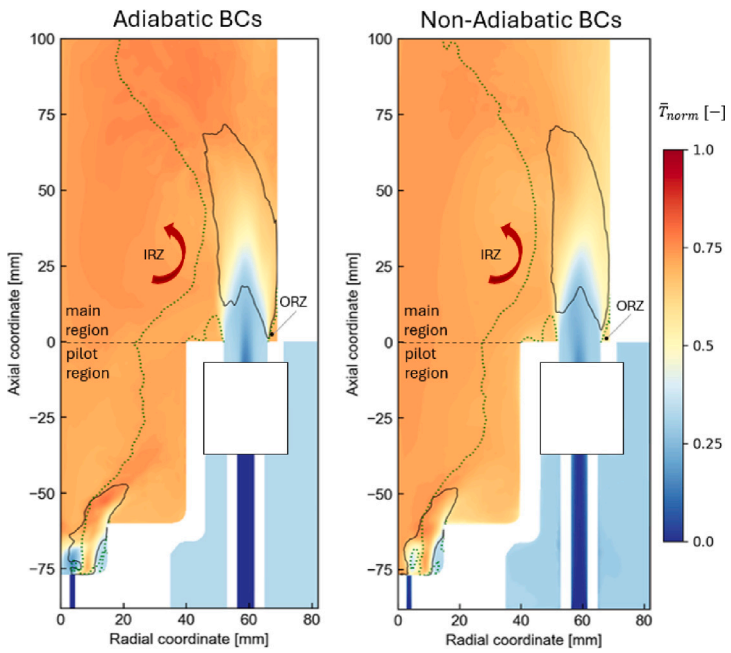

Fig. 8. Atmospheric PaSR adiabatic and non-adiabatic normalized mean temperature distributions on the midplane with superimposed mean heat release rate black isolines at 1E8 W/m and mean axial velocity green dotted isoline at 0 m/s.

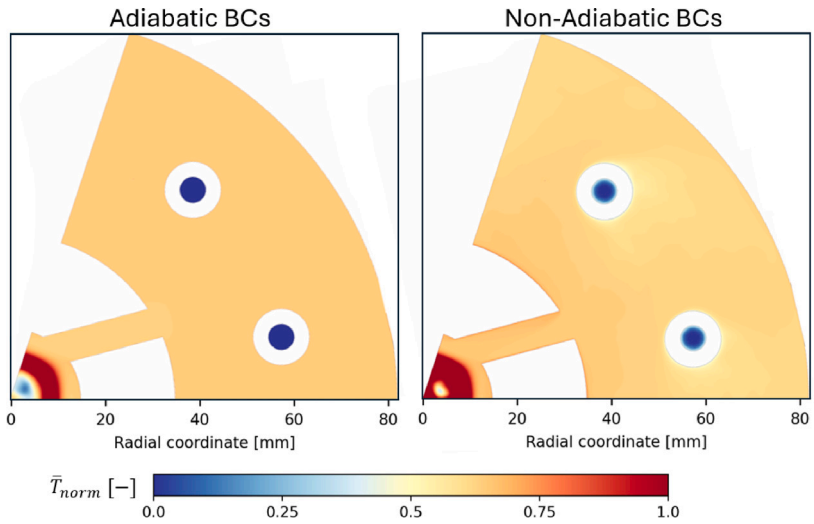

Fig. 9. Atmospheric PaSR normalized mean temperature distributions on a plane slicing the radial swirler with adiabatic and non-adiabatic thermal BCs.

As shown in Fig. 11(a), by plotting the normalized laminar flame speed, computed by solving a freely-propagating flame as a function of the mixture fraction for both H_2-Air and H_2-vitiated-air mixtures under the domain's temperature and pressure boundary conditions, the latter appears to be lower thus leading to an overestimation of the model. The vitiated-air composition was determined by calculating the species mass fractions on a constant-radius surface that vertically slices the combustion chamber (Fig. 11(b)), carefully chosen near the location where the premixed flame stabilizes, in order to account for the recirculation of products from both the pilot and main flames onto the main flame itself.

The limitation can be overcome by extending the tabulation of the fuel consumption speed to include ι, a parameter characterizing mixture dilution, as an additional control variable, yielding $S_c = S_c(Z, \beta, \kappa, \iota)$.

This parameter accounts for the influence of reduced oxygen content on the fuel consumption speed due to the oxidant dilution. ι ranges from 0 to 1, where ι=0 corresponds to an undiluted condition, with an oxygen mass fraction of 23%, typical of atmospheric air. Conversely, ι=1 represents the case of maximum dilution, wherein the oxidant is fully diluted by the combustion products, such that the resulting oxygen content matches that of the flue gases. The tabulation is achieved by iteratively adjusting the proportion of combustion products mixed into the fresh air until the target oxygen mass fraction is attained, thereby defining the corresponding dilution level.

An important aspect to consider in this context is the impact of combustion product recirculation on the main flame, from the main flame itself. This phenomenon, characteristic of the specific flow field established within the combustion chamber, can impact the main flame behavior significantly.

The dilution parameter is treated as a passive scalar, whose transport is directly coupled with the progress variable field. Specifically, its production and evolution are significant only in the vicinity of the flame front, where the progress variable approaches unity. This ensures that the dilution effect, associated with the recirculation of exhaust

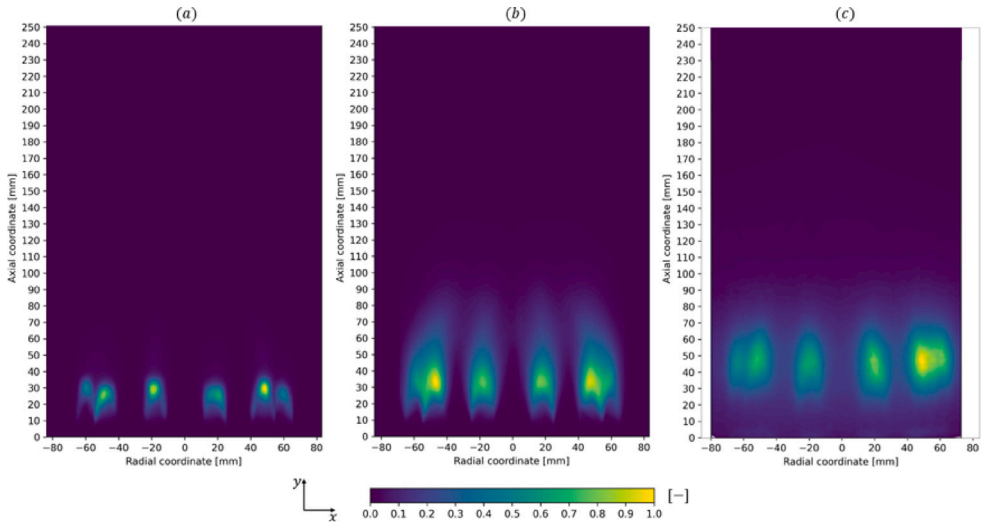

Fig. 10. Atmospheric LES-calculated LOS integrated equivalent (HRR) setting non-adiabatic thermal boundary conditions with the (a) ExtFGM Model and the (b) PaSR Model. (c) Experimental OH*-Chemiluminescence.

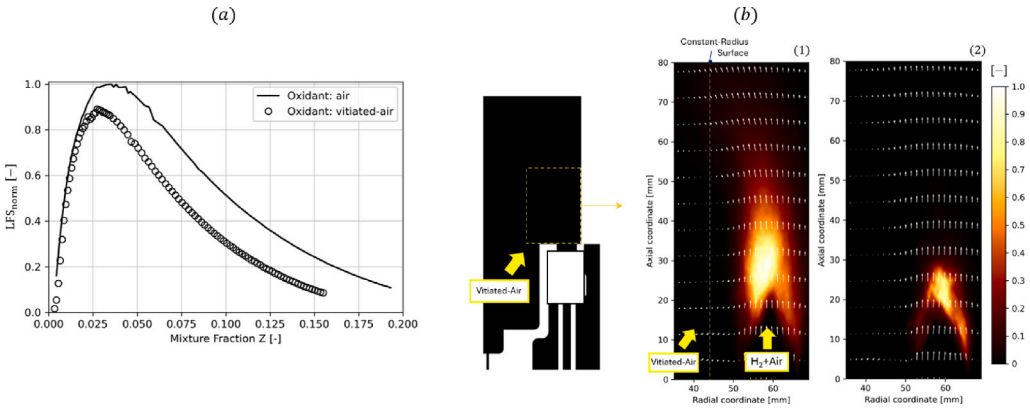

Fig. 11. (a) Laminar flame speed as a function of mixture fraction, illustrating the variation in flame speed across different mixtures. (b) Normalized mean Heat Release Rate (HRR) distribution overlaid with mean axial velocity vectors, comparing the results from the (1) PaSR and (2) ExtFGM.

gases or the introduction of inert species, is confined to regions where combustion actually occurs. As such, it provides a practical way to model the interaction between burnt and unburnt gases in turbulent reacting flows.

This modeling strategy has been widely adopted in the literature. Notably, Huang et al. [68] presented a robust extension to the FGM approach to incorporate the effects of dilution within the flamelet framework. Their work demonstrates how introducing a dilution scalar enhances the model's capability to simulate low-temperature combustion phenomena, enabling better prediction of flame stabilization, pollutant formation, and overall flame behavior in practical applications.

It is important to emphasize that this approach is only applicable under the assumption that the combustion products from both the main and pilot flames share the same composition. This ensures that their combined influence on the main flame can be consistently represented through a single dilution parameter, ι. If the composition of the recirculated products differs significantly between the pilot and main flames, representing their effects with a unified scalar would introduce modeling inaccuracies, thereby undermining the validity of the tabulated data. Consequently, the use of a single dilution parameter is justified only when such compositional uniformity is ensured, such as in the case analyzed.

In this context, the computational cost is directly influenced by the number of evaluated points across the dimensions of κ, β, Z, and ι. While adding an additional dimension to the look-up table could potentially enhance the fidelity of the combustion model, it would also significantly increase both the computational cost and the overall model complexity, particularly in the generation of the ExtFGM fuel consumption speed table. Moreover, the interpolation process, already involving three variables, would become even more computationally demanding, thereby increasing the time required to accurately compute the reaction rate correction factor, Γ.

Thus, although introducing a dilution parameter could enhance the modeling of fuel consumption speed, this extension was not implemented within the scope of the present work. Given these constraints, the inclusion of a dilution parameter is suggested as a recommendation for future work.

Another limitation of the FGM model is related to the fact that the turbulence-chemistry interaction is assumed a priori to have a β-PDF shape. This assumption may not hold accurately in high Reynolds (Re) number cases, where turbulence is more intense and a more relevant scales separation occurs. In such conditions, the simplistic assumption of a β-PDF may fail to capture the full range of turbulence effects on the flame. As a result, the interaction between turbulence and chemistry may be inadequately represented, potentially leading to an underestimation of the turbulence's impact on the flame dynamics [69].

Lastly, the current 3D implementation of the model does not account for preferential diffusion effects, particularly relevant for hydrogen due to its low Lewis number [70,71]. These effects are accurately captured in the 1D flamelet solutions using a full multicomponent

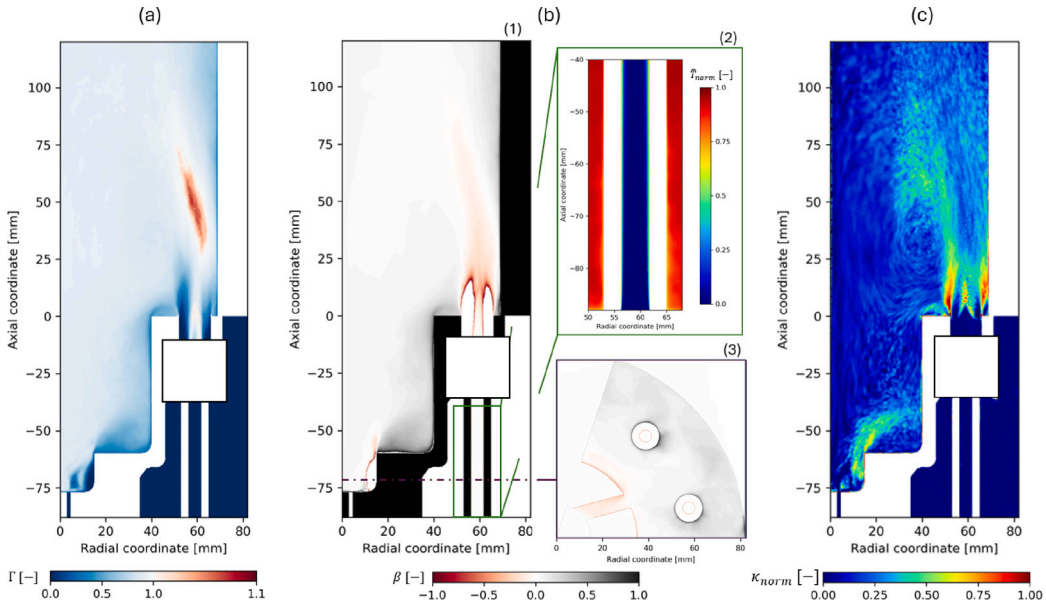

Fig. 12. Extended FGM model parameters. (a) Mean $\dot{\omega}_c$ correction factor Γ on the midplane. (b.1) Normalized mean heat loss and gain parameter β on the midplane. (b.2) Normalized mean temperature distribution in the main fuel duct. (b.3) Normalized mean heat loss and gain parameter β on a plane slicing through the radial swirler. (c) Normalized stretch κ distribution on the midplane.

transport model across varying strain rates, but are absent from the 3D simulations. One potential improvement is to assign individual mixture fractions to each species, as proposed by Kinuta et al. [72], which would enable a more accurate representation of low Lewis species behavior in the 3D framework. An alternative strategy was introduced by Swart et al. [26], who modified the transport equations of control variables by adding a diffusive term that explicitly accounts for low Lewis number effects: this approach allows the preferential diffusion contribution to be separated from the non-preferential one. Donini et al. [27] later extended this method to 3D FGM simulations, incorporating it with a progress variable, Bilger mixture fraction [43], and enthalpy as control variables. Further extensions were made by Mukundakumar et al. [73]. It should be noted, however, that none of these advanced modeling strategies were implemented in the present work.

Despite its limitations, the ExtFGM model effectively accounts for the impact of fuel pre-heating on flame reactivity. As detailed in Section 2.1, the model incorporates the effects of heat loss and gain and flame stretch on the progress variable source term $\dot{\omega}_c$, through a correction factor Γ.

Fig. 12(a) shows the Γ distribution on the midplane. A value of Γ above 1 indicates an enhancement in flame reactivity, primarily observed in the main flame region and its surrounding zone. It is important to highlight that this specific Γ distribution is closely linked to the characteristic parameters of the ExtFGM model: the heat loss and gain parameter β and the flame stretch κ.

Fig. 12(b.1) displays the distribution of β on the midplane, keeping in mind that $\beta = 0$ represents the adiabatic condition, $\beta > 0$ underlines the introduction of heat loss and $\beta < 0$ highlights the effect of heat gain. As previously emphasized, introducing non-adiabatic thermal boundary conditions reveals both temperature increases and decreases for the air and mainline fuel before entering the combustion chamber. The air is preheated due to heat transfer with the walls surrounding the pilot flame region and cooled due to heat transfer with the mainline fuel duct. Conversely, the mainline fuel is preheated as a result of heat transfer from the naturally hotter air (Fig. 12(b.1 and b.3)).

From this perspective, Fig. 12(b.2) illustrates the local temperature enhancement at the walls of the main fuel line duct. It is important to emphasize that without considering the model extension, the heat transfer effects of the mixture, directly associated with the application of non-adiabatic conditions, would not be readily observable in terms of flame reactivity. This highlights the significance of understanding the interplay between heat transfer dynamics and combustion characteristics in this context. Evaluating the β distribution on a plane slicing through the domain at the radial swirler height (Fig. 12(b.3)) reveals that the air passing through the swirler duct experiences concentrated heating, as indicated by β values less than one. Other areas are affected by generalized heat loss.

Lastly, it is crucial to assess the normalized mean stretch κ distribution on the midplane (Fig. 12(c)). High levels of stretch are found in regions of high velocities, such as in the nozzle-jet region and near the pilot flame stabilization zone. The Γ distribution reflects the stretch distribution: values of $\Gamma < 1$ are observed in high stretch areas, highlighting the reduction of flame reactivity introduced by the stretch itself.

Turning now to the evaluation based on the PaSR model, a noticeable shift emerges in the analysis. As shown in Fig. 10(b), the results obtained with this model exhibit a strong agreement with experimental data, particularly in terms of flame topology. The PaSR model successfully reproduces both the shape and length of the flame. This numerical flame pattern is further supported by experimental observations, which clearly show a bending of the flame towards the burner axis, a behavior attributed to the elevated temperature of the pilot flame products, as previously discussed in Fig. 8.

In terms of mixing dynamics, Figs. 13(a) illustrates the instantaneous equivalence ratio ϕ on the midplane for the ExtFGM and PaSR, respectively. All plots presented in these figures were computed using a common maximum value across all models, ensuring a consistent basis for comparison.

For all models, the mixture is notably fuel-rich in the nozzle region, particularly within the adduction duct and near the nozzle rim in the combustion chamber. This fuel-rich condition is primarily a result of the high jet velocities, which increase jet penetration and reduce the premixing tendency before the mixture enters the combustion chamber. However, further downstream, the main flame stabilizes in a region where the equivalence ratio decreases. In this area, turbulent structures driven by the large inner recirculation zone promote enhanced mixing, leading to a more homogeneous distribution of the equivalence ratio, ϕ.

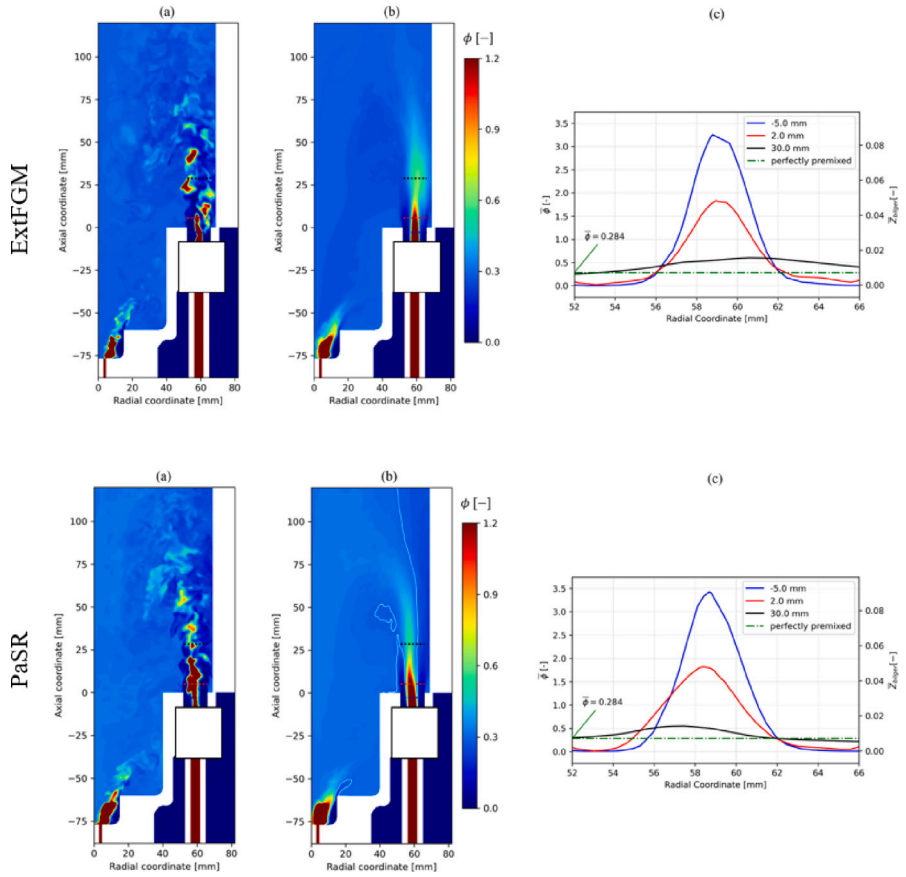

Fig. 13. Atmospheric ExtFGM and PaSR (a) instantaneous and (b) mean equivalence ratio ϕ distribution on the midplane. (c) Radial distributions of mean equivalence ratio $\overline{\phi}$ and mixture fraction $\overline{Z}$ at different axial coordinates.

In contrast, the pilot region maintains a higher equivalence ratio, ϕ, indicative of the flame's diffusive nature, as expected. The mean equivalence ratio distribution on the midplane is shown in Figs. 13(b) for ExtFGM and PaSR, with $\phi = 0.284$ isolines overlaid to represent the global equivalence ratio of the domain.

Additionally, radial profiles of the mean values of ϕ and Bilger's mixture fraction [43] for the PaSR, as well as the mean values of ϕ and the mixture fraction for the FGM model (calculated as defined in Eq. (1)), are presented in Figs. 13(c) for ExtFGM and PaSR. These profiles are shown at three distinct axial positions (−5.0 mm, 2.0 mm, and 30.0 mm) and considering both the minimum and maximum radial coordinates of the nozzle.

As previously noted, the high-momentum jets lead to the formation of a compact fuel column, which is then disrupted by the turbulent flow field within the combustion chamber. This is further corroborated by the radial distribution of ϕ, where, as the axial coordinate increases, the equivalence ratio decreases and eventually stabilizes at a constant value.

When comparing the turbulent combustion models, the PaSR model effectively captures the chemical quenching effects resulting from the recirculation of pilot flame products and their influence on the partially-premixed main flame. The increased flame lift-off observed in the PaSR model is linked to lower flame reactivity, which, in turn, is associated with a reduced laminar flame speed. This reduction is driven by differences in the oxidant composition, as previously discussed and illustrated in Fig. 11(a).

Once discussed all these different aspects, to further validate the results obtained from the PaSR model, NO_x emissions were evaluated and compared with experimental data. Additional details on NO_x emissions can be found in the previously cited work of Hohloch et al. [12].

The computational procedure for NO_x prediction was developed and validated by Amerighi et al. [74] and is based on solving the NO_x transport equations in a steady-state manner using the time-averaged LES field. This approach is particularly advantageous in terms of computational cost and efficiency, as it circumvents the need to solve transport equations for all intermediate species involved in NO_x formation chemistry.

It is also important to emphasize that this procedure was applied exclusively to the species transport-based model and not to the ExtFGM approach. In hydrogen flames, accurate predictions of velocity, mixing, and temperature are crucial for reliable NO_x estimations. The inherent limitations of the tabulated chemistry-based model would significantly impact the final results, making it unsuitable for precise NO_x predictions.

The results from the PaSR model, considering both adiabatic and non-adiabatic boundary conditions, are summarized in Table 3. The data, presented under dry conditions, corresponds to a residual oxygen content of 15 vol% and represents the mass-weighted average of the NO_x concentration at the burner outlet. Additionally, the results apply to the entire burner rather than the single sector used in the evaluation.

As shown in the table, the results align well with experimental data. Despite a slight overestimation in both the adiabatic and non-adiabatic cases, the predictions are within the same order of magnitude as the experimental values. One key observation, however, is that applying non-adiabatic boundary conditions leads to a lower NO_x concentration, underscoring the significance of including heat transfer effects in the model.

To conclude, this analysis highlights the significant impact of non-adiabatic boundary conditions and the limitations of the tabulated chemistry-based approach (ExtFGM), despite the extensions introduced to the model. The results demonstrate that the PaSR model is better

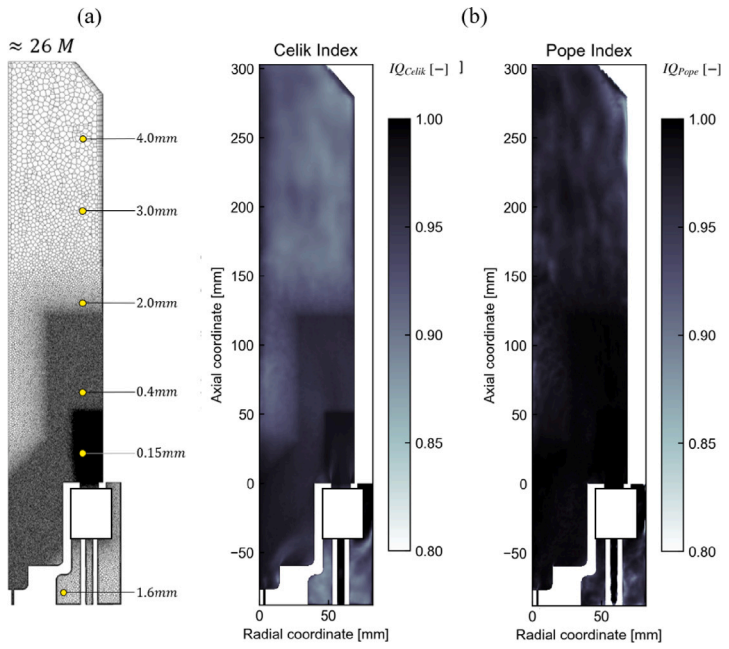

Fig. 14. (a) Computational grid for the high-pressure LES analyses, with grid sizings. (b) Contour of time-averaged (left) Celik Index [62] and (right) Pope Index [63] for the pressurized LES computational grid.

Table 3
PPM Dry NO_x corrected at the 15% of O_2 computed for the PaSR model applying adiabatic and non-adiabatic thermal boundary conditions to the burner's walls, compared to the experimental data.

	PPM NO_x 15%O_2
PaSR adiabatic	6.4
PaSR non-adiabatic	4.9
Exp	2.4

suited for evaluating the burner's performance. For this reason, this model, combined with non-adiabatic boundary conditions, was applied to characterize the same burner operating at higher pressure conditions.

4. Pressurized case

A high-pressure test was performed numerically to further characterize the burner domain and evaluate its performance under operating conditions representative of a real micro-gas turbine. As mentioned in Section 3.1, the burner was developed for the Ansaldo Green Tech AE-T100 mGT, a commercial micro-gas turbine that operates at approximately 4.5 bar. Therefore, the F400S.3 burner was analyzed under this pressure condition since eventually, the AE-T100 would be its final application.

4.1. Numerical set-up

The high-pressure LES simulations were conducted using the pressure-based code ANSYS Fluent 24R1 [42], and the computational grid for the domain, shown in Fig. 14(a), was generated accordingly. An unstructured polyhedral mesh with approximately 2.5E7 cells was created. To account for the increase in operating pressure, further refinement of the mesh in the flame region was necessary to maintain a consistent sub-grid turbulence contribution relative to the atmospheric case. This refinement was achieved using the Body of Influence (BOI) technique, which involved additional mesh refinement in the main flame region and further reduction in mesh sizing in the pilot region compared to the atmospheric configuration.

To ensure consistency in the treatment of turbulence, both the Celik [62] and Pope [63] indices were computed and their distributions are presented in Fig. 14(b). The computed indices shows comparable values in both the pilot and main flame regions when compared to the atmospheric case (see Fig. 5), confirming that the sub-grid turbulence contribution was handled consistently across both conditions.

The computational setup employed for the LES simulation perfectly replicates the one previously presented for the atmospheric case. Here, the PaSR model was applied to handle the turbulence-chemistry interaction. In fact, as shown in Section 3.3.2, the PaSR model was found to be able to better replicate the experimental results compared to the ExtFGM.

Despite an equal setup, it is important to carefully discuss the boundary conditions defined for the high-pressure case.

A pressure outlet and mass flow inlets were set as BCs for the domain. However, the higher operating pressure leads to the necessity to scale the mass flow rates to keep constant the corrected mass flow factor θ:

$$\theta = \frac{\dot{m}\sqrt{T_0}}{P_0} \tag{13}$$

where $\dot{m}$ represents the air mass flow rate, T_0 the inlet temperature and P_0 the pressure being discussed. Assuming an analogous inlet temperature, a factor of approximately 4, obtained as the ratio between the operating pressures, is identified to calculate the new air mass flow rate. Furthermore, the new mass flow rates for the pilot and main fuel line were calculated by assuming a similar global equivalence ratio $\phi = 0.284$ and a consistent fuel mass flow rate split between the two, in line with the atmospheric case.

For this case as well, non-adiabatic thermal boundary conditions were applied at the burner's walls, taking into account the heat transfer between the fluid and solid domains. As part of the pre-processing step, a RANS CHT analysis was performed also at high pressure to compute the domain walls temperature distributions. The computational setup here mirrors the one used for the atmospheric RANS CHT analysis, described in Section 3.2.

To maintain clarity and avoid over-complicating the discussion, the results of the RANS CHT analysis for the pressurized case are

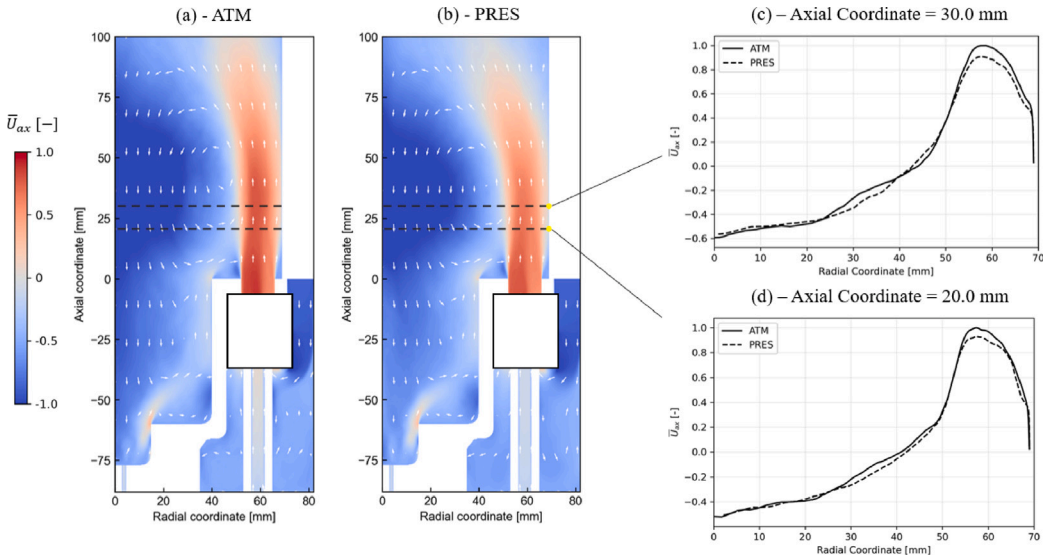

Fig. 15. Normalized mean axial velocity distribution on the midplane: (a) Atmospheric case, (b) Pressurized case, and (c) Radial distribution of normalized mean axial velocity at the 20 mm and 30 mm axial positions. Normalization was applied using a common maximum value between the two simulations.

excluded, with the focus placed on the LES outputs. The resulting temperature distribution is consistent with the conclusions drawn for the atmospheric case, underscoring the critical role of heat exchange, even under varying operating conditions.

4.2. Results and discussion

Before proceeding with the evaluation of the simulations results, it is important to reiterate that no experimental data are available for the pressurized case. The primary objective of this analysis is to assess the burner's performance at higher pressures, focusing on its ability to avoid flashback and auto-ignition.

An evaluation of the mixture velocity shows that scaling the mass flow rate does not significantly impact the mixture velocity itself, as expected. Fig. 15 presents a comparative analysis of the normalized mean axial velocity distributions along the midplane for both atmospheric (a) and pressurized (b) conditions. To ensure a consistent comparison, a common maximum velocity was selected for normalization.

In the plots, the mean axial velocity distributions are overlaid with axial velocity vectors to better highlight the recirculation zones. The results indicate that the velocity distributions remain nearly unchanged between the atmospheric and pressurized conditions, with similar axial velocities observed in the jet regions in both cases. Although a slight contraction of the IRZ is observed under pressurized conditions, the overall velocity distributions exhibits minimal variations.

Further analysis of the radial velocity profiles at representative axial positions (20 mm and 30 mm, Fig. 15(c)) confirms these findings, revealing consistent velocity profiles across atmospheric and pressurized conditions.

Fig. 16(a) illustrates the distribution of the normalized mean heat release rate (HRR) on the midplane, integrated along the line of sight (LOS) axis, as described in Section 3.3.1.

The main flame stabilizes in a region similar to that observed under atmospheric conditions, which is closely linked to the burner's jet-stabilization system. A large IRZ is formed, playing a crucial role in flame stabilization: this zone recycles hot combustion products from both the main and pilot flames, which helps sustain the flame itself.

Despite the identical computational setup, a key difference observed in the pressurized case compared to the atmospheric case is the noticeable reduction in flame lift-off height, as reported in Table 4, which also provides information on the corresponding flame length.

Table 4
Flame lift-off height (LOH) and flame length were obtained from both atmospheric and pressurized LES simulations, incorporating non-adiabatic boundary conditions at the burner walls and modeling turbulence–chemistry interaction using the PaSR model.

	LOH [mm]	Length [mm]
ATM	12	69
PRES	9	75

This reduction in lift-off height is attributed to the elevated operating pressure of the burner, which results in an increased global heat release rate. The higher heat release enhances flame reactivity and accelerates ignition chemistry, promoting flame stabilization closer to the nozzle rim and reducing the flame lift-off height. This behavior is consistent with findings in the literature, which report that increased pressure leads to shorter autoignition delays and earlier flame anchoring [75,76].

This trend is clearly illustrated in the normalized mean heat release rate (HRR) distribution on the midplane, shown in Fig. 16(b), for both atmospheric and pressurized cases. Mean axial velocity vectors are superimposed on the plots to enhance the visualization of recirculation zones, which play a critical role in flame stabilization mechanisms under both conditions.

Additional insight into this behavior is provided in Fig. 17, which presents the equivalence ratio (ϕ) distributions on the midplane, shown for both instantaneous (a) and time-averaged (b) fields.

Similar conclusions to those observed in the atmospheric case can be drawn here. The mixture is fuel-rich in the nozzle region, primarily due to the high jet velocities, which reduce the tendency for premixing before entering the combustion chamber. In contrast, the pilot region remains higher in equivalence ratio, indicative of the flame's diffusive behavior.

Examining the radial profiles of the mean equivalence ratio (ϕ) and Bilger's mixture fraction [43], shown in Fig. 17(c), it is evident that the level of premixness is significantly lower in the pressurized case compared to the atmospheric case (Fig. 13). This observation highlights the impact of operating pressure on the mixing process, where higher pressures seem to reduce the degree of fuel–air premixing before combustion. A closer examination of the radial distribution

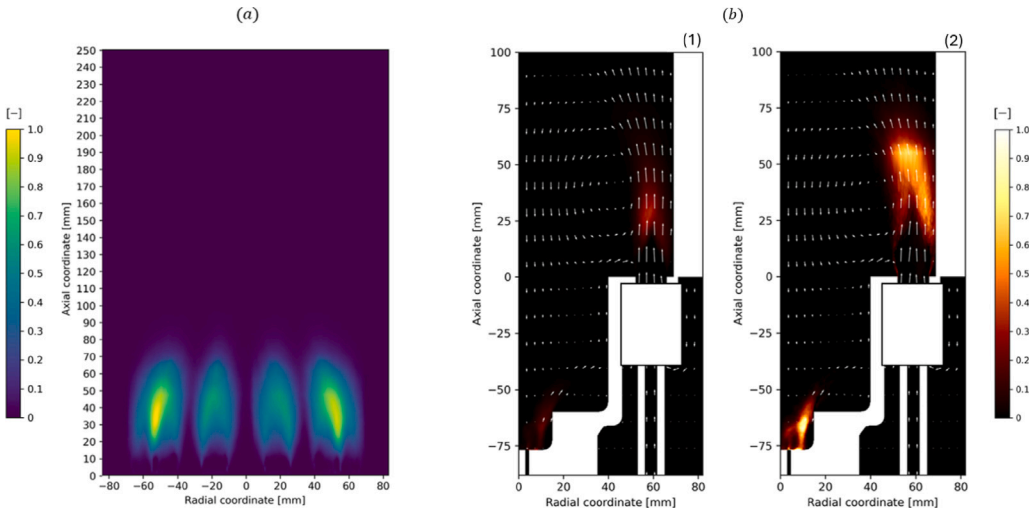

Fig. 16. (a) LES-calculated line-of-sight (LOS) integrated equivalent Heat Release Rate (HRR) for the pressurized case. (b) Normalized mean HRR distribution overlapped with mean axial velocity vectors for the atmospheric (1) and pressurized (2) cases.

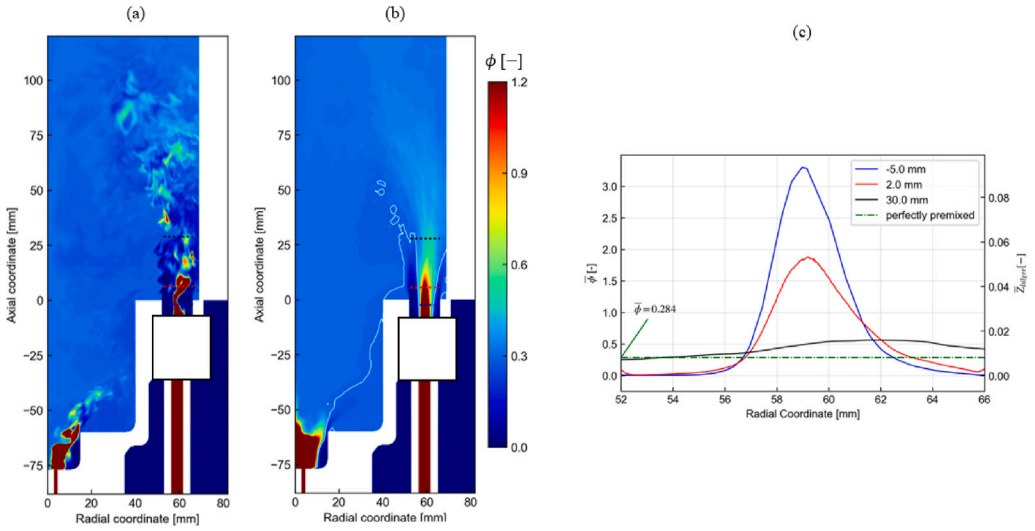

Fig. 17. Pressurized LES results: (a) Instantaneous and (b) mean equivalence ratio distributions on the midplane. (c) Radial distributions of mean equivalence ratio $\overline{\phi}$ and mixture fraction $\overline{Z}$ at different axial coordinates.

further emphasizes this difference. At various axial coordinates, the model show a higher ϕ in the pressurized case, suggesting a more fuel-rich mixture in the combustion region.

This trend is further validated in Fig. 18. As previously discussed, for the pressurized case, the flow boundary conditions were set to maintain a constant global equivalence ratio. However, the increased operating pressure induces changes in the mixing process, which subsequently leads to substantially different temperature distributions between the atmospheric and pressurized cases. These differences are clearly illustrated in Fig. 18(a) and (b) which display the normalized mean temperature contours for both the atmospheric and pressurized cases. Furthermore, Fig. 18(c) presents the normalized mean temperature profiles at 20 mm and 30 mm axial heights along the midplane, offering a detailed comparison of the temperature variations in both cases.

The temperature distributions in the atmospheric and pressurized cases are relatively similar in regions with higher mixture premixness, particularly within the IRZ, with radial coordinates lower that 40–50 mm. However, in the jet region (from 50–65 mm), where the mixture premixness is lower, notable differences emerge. As expected, a lower level of premixing results in a higher mass of fuel in the mixture, which leads to higher temperatures in the jet region.

Another important aspect for evaluating burner performance is the assessment of NO_x emissions, following the procedure previously outlined in the atmospheric pressure results Section 3.3.2. Due to the higher operating pressure, an increased NO_x level is observed: in fact, the enhanced flame reactivity determined by the higher operating pressure leads to a greater tendency for NO_x formation.

In the analyzed case, the dry NOx concentration, referenced to 15% oxygen, is approximately 37 ppm for the PaSR model. Since no experimental data are available for the pressurized configuration, a validation, at least in terms of order of magnitude, was carried out by comparing the results with literature findings. Marragou et al. [77] investigated NO_x emissions in the hydrogen-fueled academic test case Hylon, under various operating conditions, including different pressures and global equivalence ratios. Their study observed a linear increase in NO_x concentration with pressure.

In the present work, experimental NO_x values at atmospheric pressure were scaled using the same factor applied to the air mass flow rate in the pressurized burner. This approach, although simplified, provides a reference level for comparison under pressurized conditions. Despite the assumptions involved, the CFD results still capture the

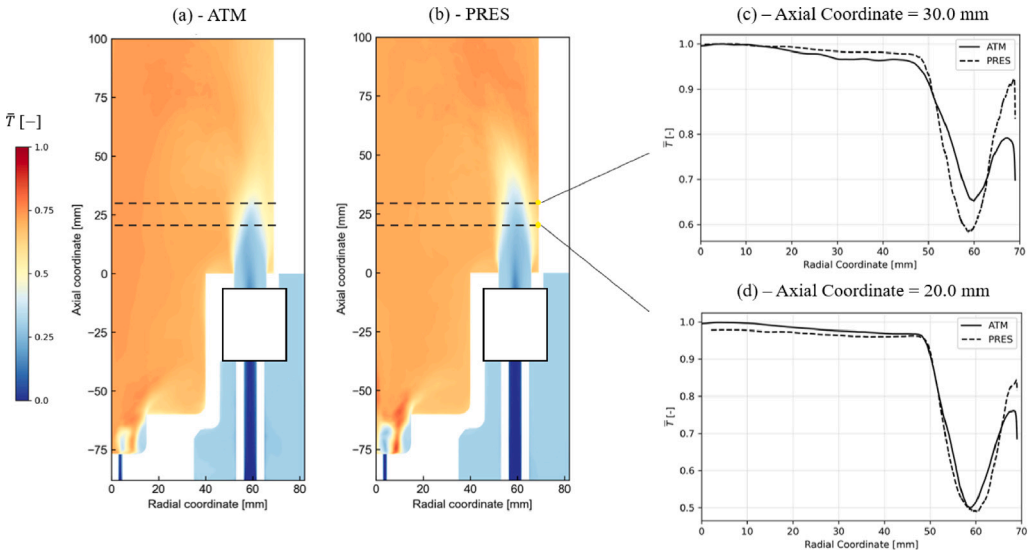

Fig. 18. Normalized mean temperature distribution on the midplane. (a) Atmospheric case. (b) Pressurized case. (c) Radial distribution of normalized mean temperature at 20 mm and 30 mm axial coordinate. Normalization was performed with a common maximum between the simulations.

correct order of magnitude, demonstrating reasonable agreement with the pressure-dependent trends reported in the literature.

To conclude, despite notable differences in flame topology compared to the atmospheric case, the burner effectively sustains stable combustion under pressurized conditions. The elevated pressure enhances certain flame characteristics, such as shape and intensity, but these changes do not compromise stability: the burner's robustness is confirmed across a range of operating pressures, mitigating potential issues like pressure oscillations and flashback.

5. Computational costs

All simulations in this study were performed on an HPC cluster composed of 16 nodes, each equipped with multi-core (48) AMD EPYC® 7413 processors.

In the RANS framework, CHT analyses were performed to resolve both the fluid and solid domains, enabling an accurate representation of thermal interactions at solid boundaries. While RANS simulations are significantly less demanding than LES in terms of computational resources, the cost remains non-negligible when detailed chemistry is involved. The estimated computational effort for the PaSR model in the RANS-CHT context was approximately 9000–11,000 CPU hours, while the RANS-CFD required between 7000–9000 CPU hours. The additional cost due to the solid domain was moderate, contributing a secondary but relevant overhead compared to the main computational load from turbulence and combustion modeling in the fluid domain.

In contrast, the LES simulations required a substantially higher computational investment. The total computational effort required, including the time-averaging phase, was estimated at approximately 28,000 CPU hours for the ExtFGM and 75,000 CPU hours for the PaSR in the atmospheric case, and 103,000 CPU hours for the PaSR in the pressurized case. The substantial difference in computational demand arises from the PaSR requirement to solve a distinct transport equation for each species involved in the reaction mechanism. As a result, for this combustion configuration, the PaSR approach incurs roughly 2.6 the computational cost compared to the ExtFGM approach.

6. Conclusions

This study presented a numerical evaluation of the jet-stabilized 100% H_2-fueled mGT burner F400S.3 under atmospheric and pressurized conditions using RANS and LES simulations. The computational setup was validated against atmospheric experimental data, then extended to high-pressure conditions representative of commercial mGT systems.

Comparisons between the PaSR and ExtFGM models showed that PaSR more accurately reproduced flame structure and reactivity, while ExtFGM, despite including flame stretch and heat-loss effects, struggled to capture flame length and lift-off. LES further highlighted the importance of non-adiabatic boundary conditions, which proved essential for correctly predicting flame topology and wall temperature distributions.

Pressurized simulations with PaSR confirmed the burner's capability to sustain stable combustion without flashback or auto-ignition. The flame stabilized closer to the nozzle, with reduced lift-off and enhanced reactivity, reflecting the stronger heat release and mixing at elevated pressure.

Overall, the F400S.3 burner demonstrated robust performance under both atmospheric and pressurized conditions. The PaSR model provided reliable predictions, non-adiabatic effects were critical at atmospheric pressure, and high-pressure operation confirmed the burner's suitability for mGT applications in terms of stability, safety, and efficiency.

7. Nomenclature

Nomenclature

Acronyms

BC	Boundary Condition
CFD	Computational Fluid Dynamics
CHP	Combined Heat and Power
CHT	Conjugate Heat Transfer
CPU	Central Processing Unit
DLR	Deutsche Zentrum für Luft- und Raumfahrt
$ExtFGM$	Extended Flamelet Generated Manifolds
HPC	High-Performance Computing
HRR	Heat Release Rate [J m^{-3} s^{-1}]
HTC	Heat Transfer Coefficient
IRZ	Inner Recirculation Zone
LES	Large Eddy Simulation
LOS	Line of Sight
mGT	micro-Gas Turbine

ORZ	Outer Recirculation Zone
$PaSR$	Partially Stirred Reactor
PDF	Probability Density Function
PSR	Perfectly Stirred Reactor
$RANS$	Reynolds Averaged Navier–Stokes
UDF	User Defined Function
Symbols	
c	Progress Variable [–]
Da	Damköhler number [–]
IQ	Celik Quality Index [–]
k	Fine-Scales Volume fraction [–]
l_t	Turbulent lenght scale [m]
l_w	Wave front lenght [m]
m	Proportionality Factor for the Γ model [–]
$\dot{m}$	Air mass flow rate [kg s^{-1}]
$n_i n_j$	Orientation Factors [–]
P_0	Operating Pressure [Pa]
$\dot{q}$	Total Heat Release Rate per unit volume [J m^{-3} s^{-1}]
$\dot{q}_{chem}$	Chemical heat release rate per unit volume [J m^{-3} s^{-1}]
q''_{wall}	Net heat flux at the surface [J m^{-2} s^{-1}]
Q_{flame}	Flame power [J s^{-1}]
Q_{wall}	Net wall heat loss [J s^{-1}]
Re	Reynolds number [–]
S_c^0	Unstretched adiabatic fuel consumption speed [m s^{-1}]
S_c	Stretched non-adiabatic fuel consumption speed [m s^{-1}]
S_l^0	Laminar flame speed [m s^{-1}]
T_0	Air Temperature [K]
Y_f	Mass Fraction of the fuel [–]
Y_i	Mass Fraction of the i-species [–]
Y_{H_2}	Mass Fraction of hydrogen [–]
Y_{O_2}	Mass Fraction of oxygen [–]
v'	Sub-grid velocity [m s^{-1}]
Z	Mixture Fraction [–]
Greek	
β	Heat Loss and Gain Parameter [–]
Γ	Extended-FR correction factor [–]
δ_{ij}	Kronencher Delta [–]
δ_l^0	Laminar flame thickness [m]
Δ	Computational Cell Dimensions [m]
ΔH_c^0	Lower Heating Value [J kg^{-1}]
ϵ	Turbulent Dissipation [m^2 s^{-3}]
θ	Corrected Mass Flow Factor [–]
ι	Dilution parameter [–]
κ	Stretch [s^{-1}]
ν	Molecular Viscosity [Pa s]
ρ	Density [kg m^{-3}]
ρ_u	Unburnt Mixture Density [kg m^{-3}]
τ	Fine-scales residence time [s]
τ_c	Chemical time scale [s]
τ_{mix}	Mixing time scale [s]
φ	Generic Turbulent Quantity
ψ	Heat loss and gain parameter [–]
$\dot{\omega}_c$	Turbulent Progress Variable Source Term [kg m^{-3} s^{-1}]
$\dot{\omega}_i$	Reaction Rate for species i [kg m^{-3} s^{-1}]
Superscripts	
$'$	Reynolds fluctuation
$''$	Favre fluctuation
$-$	Reynolds averaged
$\sim$	Favre averaged

CRediT authorship contribution statement

G. Generini: Writing – review & editing, Writing – original draft, Resources, Investigation, Formal analysis, Data curation, Conceptualization. **M. Amerighi:** Writing – review & editing. **T. Lingstädt:** Validation, Supervision. **P. Kutne:** Validation. **A. Andreini:** Supervision.

Declaration of competing interest

The authors declare the following financial interests/personal relationships which may be considered as potential competing interests: Giulio Generini reports writing assistance was provided by German Aerospace Center DLR Site Stuttgart. If there are other authors, they declare that they have no known competing financial interests or personal relationships that could have appeared to influence the work reported in this paper.

References

[1] European Commission and Directorate-General for Climate Action. Going climate-neutral by 2050 – A strategic long-term vision for a prosperous, modern, competitive and climate-neutral EU economy. Publications Office; 2019, http://dx.doi.org/10.2834/02074.

[2] Grimm F, Lingstädt T, Kathrotia T, Banihabib R, Assadi M, Kutne P, Huber A. Hydrogen and hydrogen blended jet and recirculation stabilized combustion in a turbec T100 micro gas turbine combustor. In: ETN's 11th international gas turbine conference. 2023.

[3] Maghanki MM, Ghobadian B, Najafi G, Galogah RJ. Micro combined heat and power (MCHP) technologies and applications. Renew Sustain Energy Rev 2013;28:510–24. http://dx.doi.org/10.1016/j.rser.2013.07.053.

[4] Banihabib R, Assadi M. A hydrogen-fueled micro gas turbine unit for carbon-free heat and power generation. Sustain (Switzerland) 2022;14. http://dx.doi.org/10.3390/su142013305.

[5] Murugan S, Horák B. A review of micro combined heat and power systems for residential applications. Renew Sustain Energy Rev 2016;64:144–62.

[6] Zhu S, Wang K, González-Pino I, Song J, Yu G, Luo E, Markides CN. Techno-economic analysis of a combined heat and power system integrating hybrid photovoltaic-thermal collectors, a stirling engine and energy storage. Energy Convers Manage 2023;284. http://dx.doi.org/10.1016/j.enconman.2023.116968.

[7] d'Accadia MD, Sasso M, Sibilio S, Vanoli L. Micro-combined heat and power in residential and light commercial applications. Appl Therm Eng 2003;23(10):1247–59.

[8] Petry N, Mannazhi M, Yin Z, Lammel O, Geigle KP, Huber A. Investigation of fuel and load flexibility of an atmospheric single nozzle jet-stabilized FLOX® combustor with hydrogen/methane-air mixtures. J Eng Gas Turbines Power 2023;146(6):061004. http://dx.doi.org/10.1115/1.4063782.

[9] Calabria R, Chiariello F, Massoli P, Reale F. CFD analysis of turbec T100 combustor at part load by varying fuels. In: Turbo expo: power for land, sea, and air. Microturbines, turbochargers and small turbomachines; steam turbines, vol. 8, 2015, V008T23A020. http://dx.doi.org/10.1115/GT2015-43455.

[10] Cappelletti A, Martelli F, Bianchi E, Trifoni E. Numerical redesign of 100kw MGT combustor for 100% H2 fueling. In: Energy procedia, vol. 45, Elsevier Ltd; 2014, p. 1412–21. http://dx.doi.org/10.1016/j.egypro.2014.01.148.

[11] Devriese C, Penninx G, de Ruiter G, Bastiaans R, De Paepe W. The CFD design and optimisation of a 100 kw hydrogen fuelled mGT. In: Turbo expo: power for land, sea, and air. Industrial and cogeneration; manufacturing materials and metallurgy; marine; microturbines, turbochargers, and small turbomachines, vol. 8, 2020, V008T20A004. http://dx.doi.org/10.1115/GT2020-14473.

[12] Hohloch M, Lingstädt T, Kutne P. Experimental analysis of the hydrogen capability of a fuel flexible jet stabilized syngas micro gas turbine combustor under atmospheric conditions. In: Combustion, fuels, and emissions, vol. 3B, 2023, V03BT04A039. http://dx.doi.org/10.1115/GT2023-103418.

[13] Cavaliere A, de Joannon M. Mild combustion. Prog Energy Combust Sci 2004;30(4):329–66. http://dx.doi.org/10.1016/j.pecs.2004.02.003.

[14] Lammel O, Stöhr M, Kutne P, Dem C, Meier W, Aigner M. Experimental analysis of confined jet flames by laser measurement techniques. J Eng Gas Turbines Power 2012;134(4):041506. http://dx.doi.org/10.1115/1.4004733.

[15] Banihabib R, Lingstädt T, Wersland M, Kutne P, Assadi M. Development and testing of a 100 kW fuel-flexible micro gas turbine running on 100% hydrogen. Int J Hydrog Energy 2024;49:92–111.

[16] Lammel O, Schütz H, Schmitz G, Lückerath R, Stöhr M, Noll B, Aigner M, Hase M, Krebs W. FLOX® combustion at high power density and high flame temperatures. J Eng Gas Turbines Power 2010;132. http://dx.doi.org/10.1115/1.4001825.

[17] Roediger T, Lammel O, Aigner M, Beck C, Krebs W. Part-load operation of a piloted FLOX® combustion system. In: Turbo expo: power for land, sea, and air. combustion, fuels and emissions, Parts A and B, vol. 2, 2013, p. 737–48. http://dx.doi.org/10.1115/GT2012-69006.

[18] Liu Z, Xiong Y, Zhu Z, Zhang Z, Liu Y. Effects of hydrogen addition on combustion characteristics of a methane fueled MILD model combustor. Int J Hydrog Energy 2022;47(36):16309–20. http://dx.doi.org/10.1016/j.ijhydene.2022.03.132.

[19] Oijen JV, Goey LD. Modeling of premixed laminar flames using flamelet-generated manifolds. Combust Sci Technol 2000;161(1):113–37. http://dx.doi.org/10.1080/00102200008935814.

[20] Im H, Chen J. Preferential diffusion effects on the burning rate of interacting turbulent premixed hydrogen-air flames. Combust Flame 2002;131:246–58. http://dx.doi.org/10.1016/S0010-2180(02)00405-4.

[21] Kinota K, Kai R, Kurose R. Effects of considering preferential diffusion and flame stretch in FGM method for numerical simulations of hydrogen/air flames. J Therm Sci Technol 2024;19(1):24–00087–24–00087. http://dx.doi.org/10.1299/jtst.24-00087.

[22] Puggelli S, Bertini D, Mazzei L, Andreini A. Scale adaptive simulations of a swirl stabilized spray flame using flamelet generated manifold. Energy Procedia 2016;101:1143–50. http://dx.doi.org/10.1016/j.egypro.2016.11.155, ATI 2016 - 71st Conference of the Italian Thermal Machines Engineering Association.

[23] Puggelli S, Bertini D, Mazzei L, Andreini A. Modeling strategies for large eddy simulation of lean burn spray flames. J Eng Gas Turbines Power 2017;140(5):051501. http://dx.doi.org/10.1115/1.4038127.

[24] Paccati S, Bertini D, Mazzei L, Puggelli S, Andreini A. Large-eddy simulation of a model aero-engine sooting flame with a multiphysics approach. Flow Turbul Combust 2021;106(4):1329–54.

[25] Amerini A, Paccati S, Andreini A. Computational optimization of a loosely-coupled strategy for scale-resolving CHT CFD simulation of gas turbine combustors. Energies 2023;16(4). http://dx.doi.org/10.3390/en16041664.

[26] Swart J, Bastiaans R, van Oijen J, Goey P, Cant R. Inclusion of preferential diffusion in simulations of premixed combustion of hydrogen/methane mixtures with flamelet generated manifolds. Appl Sci Res 2010;85:473–511. http://dx.doi.org/10.1007/s10494-010-9279-y.

[27] Donini A, Bastiaans R, van Oijen J, de Goey L. Differential diffusion effects inclusion with flamelet generated manifold for the modelling of stratified premixed cooled flames. Proc Combust Inst 2015;35(1):831–7. http://dx.doi.org/10.1016/j.proci.2014.06.050.

[28] Kutkan H, Amato A, Campa G, Ghirardo G, Tay Wo Chong L, Æsøy E. Modeling of turbulent premixed CH4/H2/Air flames including the influence of stretch and heat losses. J Eng Gas Turbines Power 2021;144(1):011020. http://dx.doi.org/10.1115/1.4051989.

[29] Kutkan H, Amato A, Campa G, Tay-Wo-Chong L, Æsøy E. LES of turbulent premixed CH4/H2/Air flames with stretch and heat loss for flame characteristics and dynamics. In: Turbo expo: power for land, sea, and air. Combustion, fuels, and emissions, vol. 3B, 2022, V03BT04A021. http://dx.doi.org/10.1115/GT2022-82397.

[30] Tay Wo Chong L, Komarek T, Zellhuber M, Lenz J, Hirsch C, Polifke W. Influence of strain and heat loss on flame stabilization in a non-adiabatic combustor. Eur Combust Meet 2009;(May 2014):1–6.

[31] Tay-Wo-Chong L, Scarpato A, Polifke W. LES combustion model with stretch and heat loss effects for prediction of premix flame characteristics and dynamics. In: Turbo expo: power for land, sea, and air, vol. 50848, American Society of Mechanical Engineers; 2017, V04AT04A029.

[32] Nassini PC, Pampaloni D, Meloni R, Andreini A. Lean blow-out prediction in an industrial gas turbine combustor through a LES-based CFD analysis. Combust Flame 2021;229:111391. http://dx.doi.org/10.1016/j.combustflame.2021.02.037.

[33] Klarmann N, Sattelmayer T, Geng W, Zoller BT, Magni F. Impact of flame stretch and heat loss on heat release distributions in gas turbine combustors: Model comparison and validation. Proc ASME Turbo Expo 2016;4B-2016:1–13. http://dx.doi.org/10.1115/GT2016-57625.

[34] Langone L, Sedlmaier J, Nassini PC, Mazzei L, Harth S, Andreini A. Numerical modeling of gaseous partially premixed low-swirl lifted flame at elevated pressure. In: Turbo expo: power for land, sea, and air. Combustion, fuels, and emissions, vol. 4B, 2020, V04BT04A068. http://dx.doi.org/10.1115/GT2020-16305.

[35] Ferrarotti M, Li Z, Parente A. On the role of mixing models in the simulation of MILD combustion using finite-rate chemistry combustion models. Proc Combust Inst 2019;37:4531–8. http://dx.doi.org/10.1016/j.proci.2018.07.043.

[36] Lu H, Zou C, Shao S, Yao H. Large-eddy simulation of MILD combustion using partially stirred reactor approach. Proc Combust Inst 2019;37:4507–18. http://dx.doi.org/10.1016/j.proci.2018.09.032.

[37] Iavarone S, Péquin A, Chen ZX, Doan NAK, Swaminathan N, Parente A. An a priori assessment of the partially stirred reactor (PaSR) model for MILD combustion. Proc Combust Inst 2021;38:5403–14. http://dx.doi.org/10.1016/j.proci.2020.06.234.

[38] Liu B, Li Y-x, Zhu S-h, Qin F, He G-q. Numerical investigation on flame-stabilization mechanism of supersonic-combustor-based high-temperature CO/H2 jet. Int J Hydrog Energy 2024;49:1192–204.

[39] Langone L, Amerighi M, Andreini A. Large eddy simulations of a low-swirl gaseous partially premixed lifted flame in presence of wall heat losses. Energies 2022;15(3). http://dx.doi.org/10.3390/en15030788.

[40] Castellani S, Meloni R, Orsino S, Ansari N, Yadav R, Bessette D, Boxx I, Andreini A. High-fidelity H2–CH4 jet in crossflow modelling with a flame index-controlled artificially thickened flame model. Int J Hydrog Energy 2023;48(90):35291–304.

[41] Generini G, Andreini A, Bianchi E. Combustion modelling of the T100 micro-gas turbine burner including the influence of the stretch and heat loss/gain effects on the flame. In: Turbo expo: power for land, sea, and air. Combustion, fuels, and emissions, vol. 3A, 2024, V03AT04A027. http://dx.doi.org/10.1115/GT2024-123810.

[42] ANSYS-Fluent-Solver. Theory guide. 2024, Release 24.1.

[43] Bilger R, arner SS, Kee R. On reduced mechanisms for methane-air combustion in nonpremixed flames. Combust Flame 1990;80(2):135–49. http://dx.doi.org/10.1016/0010-2180(90)90122-8.

[44] Amerighi M, Nassini PC, Andreini A, Orsino S, Verma I, Yadav R, Patil S. Assessment of flamelet generated manifold approach with inclusion of stretch effects of pure hydrogen flames. In: Turbo expo: power for land, sea, and air. Combustion, Fuels, and Emissions, vol. 3A, 2023, V03AT04A077. http://dx.doi.org/10.1115/GT2023-102651.

[45] Kathrotia T, Oßwald P, Naumann C, Richter S, Köhler M. Combustion kinetics of alternative jet fuels, part-II: Reaction model for fuel surrogate. Fuel 2021;302:120736. http://dx.doi.org/10.1016/j.fuel.2021.120736.

[46] Goodwin D, Moffat H, Speth R. Cantera: An object-oriented software toolkit for chemical kinetics, thermodynamics, and transport processes. 2018.

[47] Poinsot T, Veynante D. In: Theoretical and numerical combustion, vol. 28, RT Edwards, Inc.; 2005.

[48] Veynante D, Piana J, Duclos JM, Martel C. Experimental analysis of flame surface density models for premixed turbulent combustion. Symp (International) Combust 1996;26(1):413–20. http://dx.doi.org/10.1016/S0082-0784(96)80243-8.

[49] Veynante D, Duclos JM, Piana J. Experimental analysis of flamelet models for premixed turbulent combustion. Symp (International) Combust 1994;25(1):1249–56. http://dx.doi.org/10.1016/S0082-0784(06)80765-4.

[50] Meneveau C, Poinsot T. Stretching and quenching of flamelets in premixed turbulent combustion. Combust Flame 1991;86(4):311–32. http://dx.doi.org/10.1016/0010-2180(91)90126-V.

[51] Bray KNC. Studies of the turbulent burning velocity. Proc R Soc Lond Ser A: Math Phys Sci 1990;431(1882):315–35. http://dx.doi.org/10.1098/rspa.1990.0133.

[52] Chomiak J. Combustion: A study in theory, fact and application. Abacus Press/Gordon and Breach Science Publishers; 1990.

[53] Sabelnikov V, Fureby C. Extended LES-PaSR model for simulation of turbulent combustion. EDP Sciences; 2013, p. 539–68. http://dx.doi.org/10.1051/eucass/201304539.

[54] Li Z, Cuoci A, Sadiki A, Parente A. Comprehensive numerical study of the adelaide jet in hot-coflow burner by means of RANS and detailed chemistry. Energy 2017;139:555–70. http://dx.doi.org/10.1016/j.energy.2017.07.132.

[55] Li Z, Cuoci A, Parente A. Large eddy simulation of MILD combustion using finite rate chemistry: Effect of combustion sub-grid closure. Proc Combust Inst 2019;37:4519–29. http://dx.doi.org/10.1016/j.proci.2018.09.033.

[56] Péquin A, Iavarone S, Galassi RM, Parente A. The partially stirred reactor model for combustion closure in large eddy simulations: Physical principles, sub-models for the cell reacting fraction, and open challenges. Phys Fluids 2022;34. http://dx.doi.org/10.1063/5.0090970.

[57] Chen Z, Reddy VM, Ruan S, Doan NA, Roberts WL, Swaminathan N. Simulation of MILD combustion using perfectly stirred reactor model. Proc Combust Inst 2016;36:4279–86. http://dx.doi.org/10.1016/j.proci.2016.06.007.

[58] Golovitchev V, Tretjakov P, Raffoul C. Evaluation of drag reduction of blunt bodies at supersonic speeds by counter-flow combustion. In: 32nd AIAA fluid dynamics conference and exhibit. 2002, http://dx.doi.org/10.2514/6.2002-3296.

[59] Zornek T, Monz T, Aigner M. A micro gas turbine combustor for the use of product gases from biomass gasification. In: European combustion meeting. 2013.

[60] Zanger J, Monz T, Aigner M. Experimental investigation of the combustion characteristics of a double-staged FLOX®-based combustor on an atmospheric and a micro gas turbine test rig. In: Turbo expo: power for land, sea, and air. Combustion, fuels and emissions, vol. 4A, 2015, http://dx.doi.org/10.1115/GT2015-42313.

[61] FLOX® is a registered trademark of WS Wärmeprozesstechnik GmbH, Renningen, Germany. n.d.

[62] Celik IB, Cehreli ZN, Yavuz I. Index of resolution quality for large eddy simulations. J Fluids Eng 2005;127(5):949–58. http://dx.doi.org/10.1115/1.1990201.

[63] Pope SB. Ten questions concerning the large-eddy simulation of turbulent flows. New J Phys 2004;6(1):35.

[64] Sergeev O, Shashkov A, Umanskii A. Thermophysical properties of quartz glass. J Eng Phys 1982;43(6):1375–83.

[65] Churchill SW, Bernstein M. A correlating equation for forced convection from gases and liquids to a circular cylinder in crossflow. J Heat Transf 1977;99(2):300–6. http://dx.doi.org/10.1115/1.3450685.

[66] Kasabov P, Zarzalis N, Habisreuther P. Experimental study on lifted flames operated with liquid kerosene at elevated pressure and stabilized by outer recirculation. Flow Turbul Combust 2013;90:605–19.
[67] Shamma M, Hoffmann S, Harth SR, Zarzalis N, Trimis D, Koch R, Bauer H-J, Langone L, Galeotti S, Andreini A. Investigation of adjacent lifted flames interaction in an inline and inclined multi-burner arrangement. In: Turbo expo: power for land, sea, and air, vol. 84959, American Society of Mechanical Engineers; 2021, V03BT04A020.
[68] Huang X, Tummers MJ, van Veen EH, Roekaerts DJ. Modelling of MILD combustion in a lab-scale furnace with an extended FGM model including turbulence–radiation interaction. Combust Flame 2022;237:111634. http://dx.doi.org/10.1016/j.combustflame.2021.111634, URL https://www.sciencedirect.com/science/article/pii/S0010218021003771.
[69] Popov PP. Alternatives to the beta distribution in assumed PDF methods for turbulent reactive flow. Flow Turbul Combust 2022;108(2):433–59.
[70] Im HG, Chen JH. Preferential diffusion effects on the burning rate of interacting turbulent premixed hydrogen-air flames. Combust Flame 2002;131(3):246–58.
[71] Lee HC, Dai P, Wan M, Lipatnikov AN. Lewis number and preferential diffusion effects in lean hydrogen–air highly turbulent flames. Phys Fluids 2022;34(3).
[72] Kinuta K, Kai R, Yada K, Kurose R. FGM modeling considering preferential diffusion, flame stretch, and non-adiabatic effects for hydrogen-air premixed flame wall flashback. Combust Flame 2024;269:113718.
[73] Mukundakumar N, Efimov D, Beishuizen N, van Oijen J. A new preferential diffusion model applied to FGM simulations of hydrogen flames. Combust Theory Model 2021;25(7):1245–67.
[74] Amerighi M, Andreini A, Orsino S, Verma I, Yadav R, Reichel T, Tanneberger T, Paschereit CO. Predicting NOx emissions of a lean hydrogen flame using high and low order computational fluid dynamics models. J Eng Gas Turbines Power 2024;146(12).
[75] Takeno K, Kido H, Takeda H, Yamamoto S, Shentsov V, Makarov D, Molkov V. Flame stabilisation mechanism for under-expanded hydrogen jets. Fire 2024;7(2):48.
[76] Howarth TL, Picciani MA, Richardson ES, Day MS, Aspden AJ. Direct numerical simulation of a high-pressure hydrogen micromix combustor: Flame structure and stabilisation mechanism. Combust Flame 2024;265:113504.
[77] Marragou S, Mengu D, Es-Sebbar E-T, Magnes H, Schuller T, Guiberti TF. Flame stabilization and pollutant emissions from a H2/air dual swirl coaxial injector at elevated pressure. Int J Hydrog Energy 2025;100:163–72.